Simulation study on acousto-optics sensing of focused ultrasound

Author: Deepak Sonker

Title: Master's Thesis

Supervisors: Dr. Teemu Myllylä and Dr. Alexander Bykov

Biomedical Engineering

Faculty of Medicine

University of Oulu

2022

Sonker Deepak (2022), Simulation study on acousto-optics sensing of focused ultrasound, Faculty of Medicine, University of Oulu, Master's thesis, 62 pages.

Abstract

The acousto-optics (AO) technique can provide a good contrast with high penetration depth (upto 5 cm) and can be potentially utilized in real time monitoring of the focused ultrasound (FUS) therapies. This work presents the AO simulation study on interaction of light and FUS in single-layer brain (SLB) medium and four-layer brain (FLB) medium. FUS pressure distribution at 0.5 MHz and 0.9 MHz frequency was simulated on k-Wave toolbox and the AO Monte Carlo (MC) algorithm was developed on MATLAB to simulate the AO effect in both mediums. The result for the SLB for both ultrasound (US) frequencies suggest that the modulation depth (MD) is high in the region of US focus with a magnitude of 2%-3% and <1% at 0.5 MHz and 0.9 MHz, respectively. Moreover, the MD decreases to 5 orders of magnitude at the source region. In the FLB, the MD decreased to 4-4.5 orders at the source and was present in the skull and US focus region with a magnitude of <1% at both US frequencies. These results suggest that AO can be utilized in sensing FUS effects to brain tissue and the AO signal-to-noise ratio (SNR) depends not only on the MD but also on the level of light intensity interacting with the US pressure.

Keywords: Acousto-optics, Focused ultrasound therapy, Modulation depth

Foreword

The thesis is a culmination of my work I did in Myllylä lab at the University of Oulu. First and foremost, I will thank my supervisors Dr. Teemu Myllylä and Dr. Alexander Bykov for providing me the opportunity to work in OPEM. One thing I liked about Teemu is the freedom he provides to his students in doing research which gave me a sense of responsibility about my research and its results. Furthermore, special thanks to Alexander who gave me his valuable time for long hour discussions on Monte Carlo and acousto-optics simulations. These discussions were very helpful in strengthening my basics in simulating light propagation in tissues. I would also like to thank Dr. Zuomin Zhao for providing me the experimental knowledge in acousto-optics, ultrasound transducers, and phantom development. Moreover, I would like to thank Dr. Hany Ferdinando for helping me to perform simulations on the Puhti server. I had a very nice time at OPEM especially I would like to acknowledge Sadegh Moradi who was always ready for the discussions and one thing I learnt from him is about the working of lock-in detector.

Lastly, I would like to thank my father and brother who showed trust over my decision of pursuing higher education from Finland. Specially, I would thank my grandmother who's "always aim high" approach is the result where I am right now and this thesis is dedicated to her…..

Oulu, May 2, 2022

Deepak Sonker

Abbreviations

MRI	Magnetic resonance imaging
CT	Computer tomography
PET	Positron emission tomography
SPECT	Single-photon emission computed tomography
BBB	Blood brain barrier
PA	Photoacoustics
AD	Alzheimer disease
ALS	Amyotrophic lateral sclerosis
PD	Parkinson's disease
OCT	Optical coherence tomography
DOT	Diffuse optical tomography
CCD	Charged coupled devices
HIFU	High intensity focused ultrasound
DCS	Diffuse correlation spectroscopy
FUS	Focused ultrasound therapy
LIFU	Low intensity focused ultrasound,
CNS	Central nervous system
CSF	Cerebro-spinal fluid
UCA	Ultrasound contrast agent
MC	Monte Carlo
AO	Acousto-optics
TRUME	Time-reversed ultrasound microbubble encoded
TRUE	Time-reversed ultrasound encoded
ARF	Acoustic radiation force
RTE	Radiative transport equation
PRC	Photorefractive crystal
MCX	Monte Carlo Xtreme
UFP	Ultrasound field perturbation
PMT	Photo-multiplier tube
MARD	Mean absolute relative difference

PAT	Photoacoustic tomography
PML	Perfectly matched layer
MD	Modulation depth
MHz	Mega hertz
kHz	Kilo hertz
MPa	Mega Pascal
PCS	Pressure contrast signal
US	Ultrasound
GPU	Graphics processing unit
SNR	Signal-to-noise ratio
SLB	Single-layer brain
FLB	Four-layer brain

List of Symbols

s	Step size
L	Thickness
v_a	Speed of US
ρ	Acoustic density
p	Acoustic pressure
ρ_0	Equilibrium density
α	Absorption coefficient
α_0	Power law prefactor
ω	Angular frequency
Y	Power law exponent
c_0	Isentropic sound speed
l_{tr}	Transport mean free path
u	Acoustic particle velocity
μ	US attenuation coefficient
L	Linear integro-differential operator f
d	Acoustic particle displacement
$\widehat{\Omega_x}, \widehat{\Omega_y}, \widehat{\Omega_z}$	Direction cosine of photon
$\widehat{\Omega_x}', \widehat{\Omega_y}', \widehat{\Omega_z}'$	Updated direction cosine
$\phi_{d,j}(r, t)$	Phase due to scatterer displacement
ω_0	Optical angular frequency
ζ	Random number
n	Refractive index
τ	Lag time
Φ	Local initial phase
μ_s	Scattering coefficient
g	Anisotropy coefficient
η	Elasto-optic coefficient
μ_t	Interaction coefficient
θ	Polar deflection angle
n_0	Initial refractive index

k_a	Wave number of ultrasound
ω_a	Acoustic angular frequency
φ	Azimuthal deflection angle
$\widehat{\Omega}_{sc}$	Scattered photon direction
Δn	Change in the refractive index
$\widehat{\Omega}_{inc}$	Incident direction of photon
$R(\phi_i)$	Fresnel reflection coefficient
μ_a	Absorption coefficient
$\lvert\phi_{us}\rvert$	Magnitude of phase shift
$\angle\phi_{us}$	Angle of phase shift
$E^*(\mathbf{r}, t-\tau)$	Conjugate of the electric field
$G(\tau)$	Autocorrelation function
Δx, Δy, and Δz	Spacing between grid points
$E_s(r, t)$	Electric field of a single path
$A_s(r)$	Amplitude of the electric field
$\phi_{m,s}$	Phase due to random fluctuation
J_0	Bessel function of first kind of order zero
J_m	Bessel function of first kind of order m
$\phi_{n,i}(r, t)$	Phase due to refractive index change
$\phi_{us}(t)$	Total ultrasound induced phase modulation
$\widehat{\Omega_a}$	Direction of ultrasound propagation
$M_{0,n}$	Unmodulated light ($M_{0,n}$) of the power spectrum
$M_{1,n}$	Modulated light ($M_{0,n}$) of the power spectrum

Table of contents

1 Introduction

There are various non-invasive imaging techniques in biomedicine like Magnetic resonance imaging (MRI), Computer tomography (CT), Positron emission tomography (PET), Single-photon emission computed tomography (SPECT) and US which are useful in diagnosing the altered functions of the human body. However, they are cumbersome and use ionizing radiation and lack contrast. On the other hand, optical imaging is non-ionizing in nature and can provide physiological information of tissues. Moreover, optical properties of biological tissues are related to the molecular constituents of tissues in visible and near-infrared range. The absorption coefficient of the tissues depends on the wavelength of light which helps in spectroscopic and functional imaging of tissues. However, the limiting factor of high-resolution imaging is the strong absorption and scattering of light in biological tissue which restricts deep penetration of light. Few optical imaging techniques are used in tissue imaging, such as, optical coherence tomography (OCT) that detects the ballistic photons at an imaging depth of ~1- 2 mm and diffuse optical tomography (DOT) that can reach a higher depth of up to 5 cm but provides poor resolution of image due to low number of detected photons [1], [2]. To overcome all these problems another branch of optical imaging i.e., hybrid imaging techniques are currently being developed. One of them is the photoacoustics (PA) that uses short light pulses to irradiate the tissue and the PA waves are excited due to thermoelastic expansion. These PA waves are detected by the wideband US transducer and are used to reconstruct the optical absorption distribution [3]. The other is acousto-optics (AO) that combines the advantage of optical imaging (i.e. its contrast) with the US which has high penetration depth, low scattering and good spatial resolution. AO was first theorized by Brillouin and later Debye et. al. and Lucas et. al. independently proved the phenomenon experimentally [4]. Raman and Nath gave the analytical model of AO effect -also called Raman-Nath diffraction- in homogeneous non-absorbing and non-scattering medium [5]. But the application of AO in biological imaging was first demonstrated by Marks et. al. where they demonstrated the possibility of imaging a homogenous turbid media by detecting US modulated light using a single pin photodiode detector [6]. Later, Wang et. al. obtained 2D images of object in phantom of turbid media using AO [7] and Luez and Maret gave an analytical model of AO effect and tested their theory [8]. Leveque et. al. developed a

parallel detection technique for AO signals using CCD camera and obtained 1D images of buried objects in biological tissues [1]. In all above models, US is focused to the sample and light is incident on the focal region of the US, causing modulation of light and the detection of modulated photons provide the information of optical properties of the sample with US resolution. The analytical model of AO effect was developed by Wang for the homogeneous scattering medium and later he also provided the Monte Carlo (MC) simulation of his theoretical model [9], [10]. The analytical models containing AO modulation using continuous and pulsed US were developed for anisotropically scattering media [11], [12]. Till now, there are number of developments which took place in the AO field like high intensity focused ultrasound (HIFU) real time monitoring [13], AO along with photoacoustic tomography (PAT) was used for fluence correction and artifact reduction and also obtained oxygenation in blood samples [14], a technique called AO ptychography developed recently which allows optical diffraction-limited imaging [15], in one of the techniques speckle decorrelation was used to image beyond the acoustic diffraction limit using AO [16], AO is utilized for deep tissue gated microscopy [17]. Recently, AO imaging through human skull has been made feasible [18]. AO has also been combined with diffuse correlation spectroscopy (DCS) to estimate the perfusion at different depths in tissue [19]. Moreover, AO is also used in imaging and sensing blood flow deep inside a highly scattering medium [20]. Also, there has been a wide development of AO detectors including CCD cameras, Fabry-Perot interferometers, photorefractive crystals, heterodyne digital holography, and spectral hole burning for efficiently detecting the minute modulated signal [14].

The objective of the thesis is to study through modelling and simulation the AO effect in presence of focused ultrasound (FUS) in the FLB medium. The thesis flow is as follows: The first chapter is about the introduction of FUS and AO and some current studies on AO in biomedicine. The second chapter deals with the background of the US therapy and AO effect with their uses in general. Next, we will talk about the ultrasound and optics simulation and how they are combined into one as acousto-optics Monte Carlo (AO-MC) model in chapter three. The results followed by discussion is given in chapter four and five, respectively. Chapter six deals with conclusion and future work.

2 Background

2.1 Focused Ultrasound Therapy

2.1.1 Introduction to US and its role in medical therapy

Since the advent of ultrasound (US) usage in medicine in 1960s [21], it has played a vital role in facilitating sonographers in diagnosis of anomalies inside our body. Due to its advantage of non-ionizing and harmless nature, there has been a constant development of US and it is still one of the most active research areas for the last 30 years. The miniaturization of electronic components made way for development of different types of ultrasound transducers and good as well as fast imaging systems. Today, US research is going on in numerous areas like Doppler US, elastography, super resolution imaging, 2D array transducers, echo cardiography, hybrid imaging techniques, etc. [22].

Along with the development of US imaging there was also a parallel and constant development of therapeutic US in medicine since 1927 and recent development of transducers (phased array transducers) has accelerated the development in this area. It was found that using US frequency range from 20 kHz to 10 MHz induces changes in biological tissues and can alter the mechanisms of cells, microbes, etc. At these frequencies the therapeutic US can be classified into two types: low intensity (0.125-3 W/cm^2) and high intensity (>= 5 W/cm^2) [23]. The lower intensities are used to stimulate the transport of drugs in the membrane, induce physiological response to injury, or to trigger neuromodulation whereas, high intensity US is used for tumour ablation, lithotripsy or sonoporation.

2.1.2 Effect of US on tissue

There are two kinds of mechanism involved with the use of therapeutic US, they are the thermal and non-thermal effects. However, there is no fine line to separate these two effects and they can occur simultaneously.

2.1.2.1 **Thermal effect**

The incident US wave in tissue experiences attenuation and the subsequent transmission waves has a reduced energy which can be related as, $I(z) = I_0 * \exp(-\mu z)$, here, I(z) is the

reduced intensity, I_0 is the incident intensity, z is the depth and μ is the attenuation coefficient. The heating of tissue is due to absorption of US waves. The rate at which the temperature rises is given by, $Q = \frac{\mu * I}{\rho * C}$ where, μ is the intensity attenuation coefficient, ρ is the density of the tissue and C is the specific heat capacity of tissue. This relation holds on an assumption that all the attenuated energy is due to the absorption of the US waves. It is to be noted that 60-80% of total attenuation is due to absorption. The thermal effects of US are utilized in various therapies including physiotherapy, increasing cellular enzymatic activity, blood flow, permeability, and elasticity of cellular membrane. When temperature induced is very high it can be beneficial in high intensity focused ultrasound (HIFU) tumour ablation related therapies [24], [25].

2.1.2.2 **Non-thermal effects**

The non-thermal effects of US are considered beneficial in the therapeutic usage and can induce temperature up to 1 ℃. The non-thermal mechanisms are divided in two categories:

i) Non-inertial Cavitation: The acoustic cavitation mechanism is induced when moderate or ow alternating pressure in US causes gas bubbles (present inside the tissue) to oscillate around its equilibrium position with the pressure without collapsing. This form of cavitation is known as stable cavitation and when generated causes current flow in surrounding fluid (known as microstreaming) and causes mechanical stress in cells which in turn induces biological response.

ii) Inertial Cavitation: If pressure amplitudes are increased it causes non-linear oscillations which results in collapse of gas bubbles. This kind of cavitation is also known as unstable cavitation and produces shock waves in surrounding liquid due to bubble's violent collapse. Moreover, the violent collapse causes adiabatic process of gas inside the bubble which increases the temperature and pressure significantly leading to production of free radicals and light emission (sonoluminescence). In solid surfaces (like stone, metal, cell wall) the pitting of the surface is seen due to high-speed liquid microjet formation by the

inertial cavitation effect. This mechanism helps in disintegrating kidney stones during lithotripsy [25], [26].

2.1.3 Types of Ultrasound Therapies and their medical application

The categorization of US therapies is based on the acoustic intensities used. Based on the criteria there are two kinds of ultrasound therapies namely HIFU and low intensity focused ultrasound (LIFU).

2.1.3.1 **HIFU**

The HIFU technique uses continuous US at 0.5 – 3.5 MHz frequency range for short time usually in seconds. Unlike the conventional US imaging, HIFU utilized high range of amplitudes and intensities typically in the range of 10 – 30 MPa and 1 – 10000 W/cm^2 respectively. HIFU is generally used for ablation by precisely focusing the US beams deep inside the tissue, this focusing causes acoustic energy deposition at a specific point resulting in temperature rise of over 60 – 80 ℃ in few seconds causing tissue necrosis, protein denaturation, tumour cell killing at that focal spot. Also, along with the thermal effect, high temperature induces inertial cavitation which further damages the targeted tissue through apoptosis. Furthermore, histotripsy is one area where non-inertial cavitation is used for rapid mechanical ablation with high energy of ultrashort US pulses. US beam is delivered by concave transducers or phased array transducers and the focal point is determined by the mechanical movement of the transducer with electronic steering of US beam is used for fine control of the focal spot location [27].

Monitoring of HIFU

The real time monitoring during HIFU for safety and guidance is done by:

i) MRI: It provides accurate planning of the target tissue due to its high anatomical resolution and sensitivity for tumour detection. The MR guided US therapy is currently used in research and clinical studies. Also, with MR thermometry it is possible to get real time temperature at the focal site during sonication. However, MRI is expensive, bulky and its temporal and spatial effects can lead to underestimation of temperature [27].

ii) US: The US technique is currently in research phase. US monitoring of HIFU is usually more convenient than MRI because it provides acoustic window for

verifying the efficacy of HIFU in real time. But the inability to evaluate intra-procedural therapeutic boundaries is the limitation of US monitoring [27].

iii) Photoacoustic Imaging: It is a hybrid imaging technique which is in the development phase and has a potential to evaluate real time monitoring of HIFU. It can measure the extent of ablation by providing the information about the oxygenated and deoxygenated state blood vessels around the induced lesion. Multispectral Photoacoustic can provide the differences between the spectrum of treated and untreated lesions [28], [29]. The photoacoustic imaging system for HIFU is currently in research phase.

iv) Acousto-optics: It is another hybrid imaging technique which can provides a real time monitoring of HIFU. It has the potential to quantify the optical properties of tissues which can give the information about the extent of damage caused in real time setting [30]. The AO HIFU system is currently in research phase.

Limitation and problems associated with HIFU

HIFU is sensitive to patient movement, near field heating and has a long treatment time. There have been reported cases of burns and second degree burns in treatment of renal calculi by shock wave lithotripsy. Also, there are side effects like pain, nausea, and wounds. There were cases of undesirable tissue injury, unwanted burns due to no real time monitoring of extent of ablation. HIFU can rarely cause impotency and incontinence during prostate cancer treatment. Also, there are cases of fistula formation and rib necrosis associated with HIFU treatment of hepatic and pancreatic cancer treatment [27].

2.1.3.2 **LIFU**

It is a non-ablative US therapy which utilizes pulsed US at an intensity level less than 3 W/cm^2 having a duty cycle of 20% or 50%. The Figure 1 shows the LIFU technique being used for brain therapy. There is low thermal effect as compared to HIFU and the vibration due to LIFU causes stable cavitation and the formation of acoustic streaming facilitates the displacement of small molecules and ions resulting in disruption of membrane permeability diffusion rates [31]. The applications of the LIFU are -

i) Blood Brain Barrier (BBB) disruption and targeted drug delivery

The mechanism: It is the cellular boundary between the blood and the central nervous system (CNS). It is composed of capillary endothelial cells which are tightly fused by tight junctions. The BBB acts as a filter which obstruct the diffusion of microscopic objects like bacteria, large molecules, etc into the cerebral spinal fluid (CSF) while it allows diffusion of small hydrophobic molecules. This selective nature of BBB poses a challenge to deliver 98 % of therapeutic drugs (which are useful in treatment of brain related ailments) cannot pass into CSF or parenchyma of brain. In 2001 [32] showed that using LIFU with intravenously administered microbubbles can cause reversible BBB opening without tissue damage.

For the BBB related FUS therapy, commercially available ultrasound contrast agent (UCA) is injected to patient, these UCA contains high concentration of microbubbles. These microbubbles (1 -10 um) have gas inside the albumin or lipid shell. When short burst of FUS beam is incident on these microbubbles they tend to undergo stable cavitation. Additionally, it is observed that these oscillation produces microstreaming and which in turn causes shear stress on the endothelial cell walls, creating opening of BBB. This mechanism causes non-invasive and safe permeation of large molecules into the CSF [31].

The ability of FUS mediated microbubble opening of BBB has opened a new direction from drug delivery into the brain (especially chemotherapeutics) to viral vector-based gene therapy (ex adeno-associated virus (AAV)). In a recent study it is shown that the FUS - BBB with microbubbles can be used in Parkinson's disease dementia [33], [34].

Tissue effects due to FUS induced BBB disruption

- FUS and microbubble parameters influence the magnitude of BBB permeability and the extent of tissue damage [34]
- There are changes in vascular permeability, but more studies are needed due to the complexity involved in the mechanism and some cases of inflammation were reported [35].

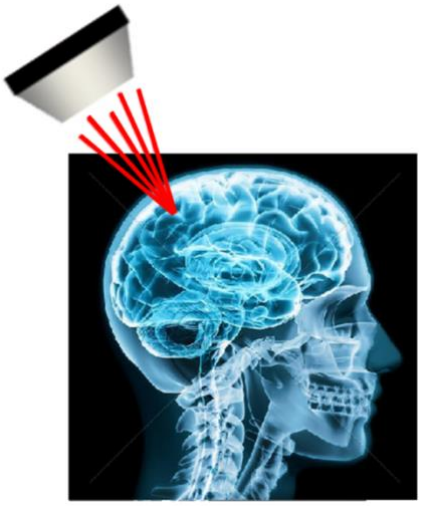

Figure 1 The low intensity FUS for brain US therapy [72].

ii) Neuromodulation

The mechanism: It has been long noted that sound pressure can affect brain tissue through mechanical displacement, heating, and cavitation. However, there are several mechanisms in which FUS affects electrical activity of the brain. One of the mechanisms stated that the alteration of electrical activity is due to mechanical forces exerted by the US pressure on mechano-sensitive ion channels. Also, later it was empirically seen that when the mechano-sensitive ion channels were removed there was no response to FUS on neural activity. Furthermore, there is another complex mechanism which posits that the FUS causes formation of bilayer sonophores (a bi-layer phospholipid membrane). These layers could generate capacitive displacement currents which can affect activity of brain. However, there is a need of physiological proof for these mechanism as well as the underlying cause of FUS induced neuromodulation which is still an open question [36], [37].

2.1.4 Applications of US therapy

US stimulation onto peripheral nerve can produce muscular contraction by modulating action potential. Additionally, transient reversible effects from tens of millisecond to 90 min exposure to FUS cause different kinds of neuromodulation, like fast-acting effects causes activation of voltage-gated sodium and calcium channels whereas, ultrasound waves can cause displacements of 1 to 3 microns in-vivo in primate brains which can alter

membrane properties and can further cause neuromodulation. There is also evidence that FUS pulse can cause auditory activation. Moreover, FUS-induced can inhibit and enhance neural activity in superficial and deep brain regions. In healthy individuals it was shown that sonication of visual cortex can evoke phosphenes. There is a clinical prototype Neurolith which is a transcranial pulse stimulation system used for neuromodulation and has an optical tracking system for navigation [34], [37].

2.1.5 Uses of FUS in neurodegenerative diseases

i) Alzheimer disease (AD)

It is characterized by progressive cognitive decline resulting from widespread neurodegeneration. One of the pathological hallmarks of AD is the accumulation of beta amyloids in the brain. Numerous studies have shown that FUS mediated drug delivery by inducing BBB opening has enhanced the pathological clearance of proteins and reduction of amyloid plaque load in the brain. Furthermore, recent study has demonstrated the safety and feasibility of transient BBB opening within the hippocampus in people with early AD and the next phase of trial will combine the FUS-BBB opening with therapeutic agents to directly target the AD pathology [34].

ii) Amyotrophic lateral sclerosis (ALS)

Patients suffering from ALS experiences loss of muscle activity due to lower and upper motor neuron degeneration. There are various evidence that using FUS-BBB opening to deliver growth factors, or genes, or cell therapies targeting primary motor cortex can be an effective treatment of ALS. Recently, using FUS-BBB open-label study on four patients having ALS were tested and the outcome of the study showed that there no acceleration of disease progression seen [38].

iii) Parkinson's Disease (PD)

The parieto-occipito-temporal junction is a prominent site for cortical pathology in PD which is linked with the main cause of cognitive impairment. The BBB restricts many drugs from gaining access to this site in brain.

However, FUS-BBB in combination of injected microbubbles can temporally open BBB which can effectively provide drugs to the targeted brain regions. Recently, phase I trials reported safe, feasible, and reversible FUS-BBB opening and mild cognitive improvement with no side effects was observed after the treatment [38], [39].

iv) Neuro-oncology

Glioblastoma is the most fatal of all cancers and no increase in life expectancy has been reported since the adoption of treatment protocol in 2005. One of the major issues in this cancer is the drug's inability to penetrate the BBB and immunosuppressive glioblastoma microenvironment enables tumour cells to evade immune system. These problems can be dealt by using FUS-BBB opening which could detect tumour cells and can trigger antitumour immune response. Furthermore, FUS-BBB opening can also be beneficial in gaining insights into the function and structure of human glymphatic system, which is a microscopic waste clearance system of brain like the lymphatic system of body [39], [40].

2.2 The Acousto-optics effect

A transmitted light from a tissue sample when detected forms a speckle pattern due to the interference of light having different phase differences. However, when US is introduced in the medium, the frequency of light gets modulated or "tagged" as it passes through US focused region as shown in Figure 2. This modulation of light causes blurry and varying speckle pattern due to time varying US and the detected speckle's frequency spectrum contain n orders of sidebands where the zeroth order is the untagged light. Also, the detected signal is very minute in comparison to untagged light [1]. The tagging of light in the medium can be categorized into three possible mechanisms: The first is the displacement or oscillations of scatters by the US waves, scatterers oscillating at US amplitude causes variation in optical path and that in-turn causes phase variation in light. In the tissue where light is multiply scattered, this mechanism causes accumulation of phase variations and consequently, the intensity of speckles varies with the US frequency. The first mechanism is only valid when the mean free path is much greater than the acoustic wavelength. In addition to the first mechanism, the second mechanism describes

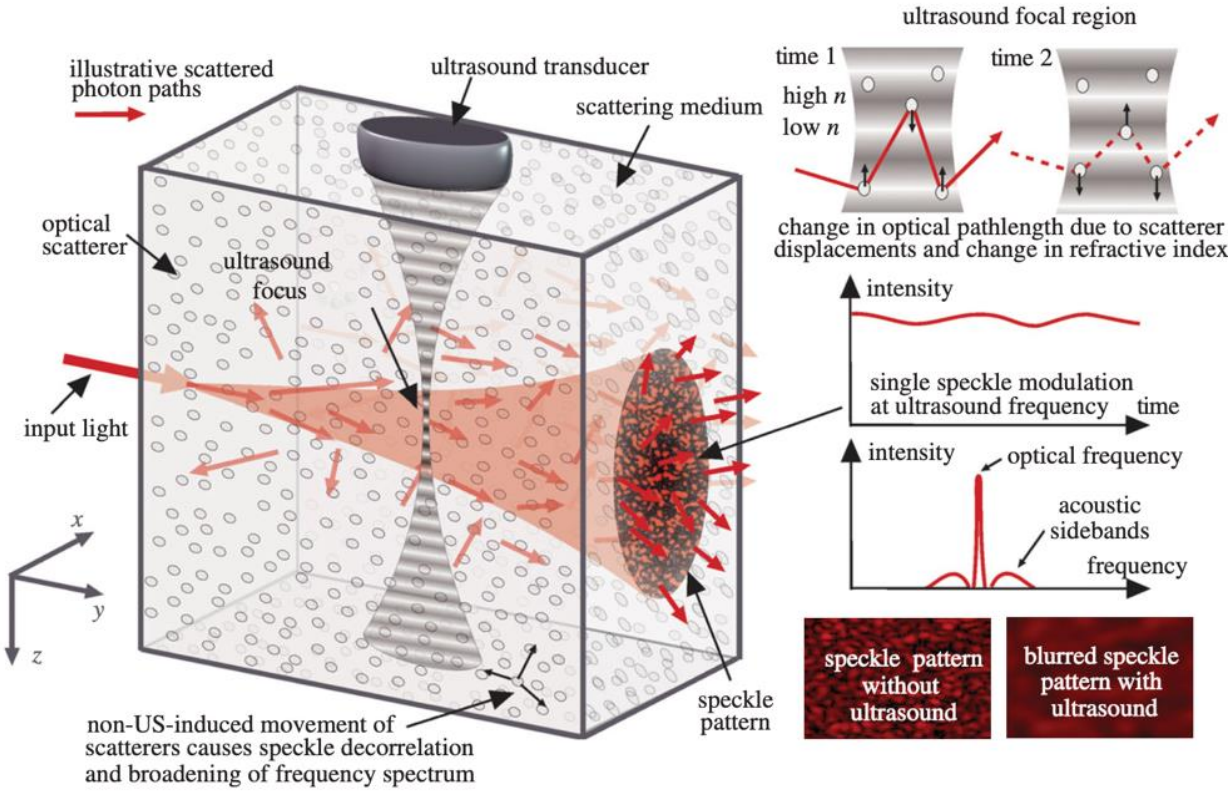

Figure 2 The complete mechanism of AO generation and the detected speckle pattern [2]. Reprinted by permission from the Royal Society (U.K.).

the phase variation due to the change in refractive index between the scattering events. And the third mechanism is due to change in optical properties– the absorption coefficient, the scattering coefficient, and the index of refraction - of the medium due to the ultrasound perturbation. It is noted that the first two mechanisms require a coherent light source while the third mechanism doesn't however the US modulated signal of incoherent light is very weak and so the third mechanism is neglected in modelling of AO effect [41]. Recently, when the pulsed US is used and if the particles move with the background fluid in the medium then the first two mechanisms are not independent, and this can affect the extent of light modulation and tagging efficiency. In other words, the two US modulation mechanisms counteract each other with the background movement of particles [42], [43].

2.2.1 Modelling and simulation studies

To gain more insight into the tagging mechanism, light modulation in tissues can be accurately studied by employing MC. The AO MC model simulates US tagging of

photons inside the medi um and was first developed by Wang for homogeneous media and was later verified by the analytical model [10]. Moreover, AO MC model for inhomogeneous and multiply scattered light was developed [11]. The time required to simulate large number of photons is quite long so to deal with this problem AO MC model was developed for GPU processors by Leung and Powell [44]. Their GPU model matched well by the analytical model and was faster than the CPU version. Adam et. al. introduced AO modeling for HIFU monitoring in which they used MC to determine design parameters of HIFU AO guided system [45]. Furthermore, Honeystt et. al. incorporated MC model for simulating AO with microbubbles [46]. There is also other MC model to study the perfusion effect on US modulated light, improving US focus inside the turbid media [4]. Recently, a COMSOL model to simulate AO in double-layered tissue was developed [42]. The authors showed that the AO signal is like US wave and has periodic variation as the US frequency changes. Moreover, the AO signal is affected by the optical properties of the double-layer medium. However, the modulation depth only depends on the optical properties of the tissue at the US focal zone.

2.2.2 Review on research techniques of AO

The US modulated signal is very weak compared to the background DC signal, so the goal of different detection techniques is to improve the AO signal by tweaking different US side techniques for better resolution. On the other hand, the development of optical side techniques is done to enhance the SNR of detected AO signal. The different methods for the two sides are [4].

2.2.2.1 **Ultrasound techniques**

i) Dual-frequency ultrasound

This technique is employed in different ways such as by using a confocal two-region US transducer, delaying two US pulses of different frequencies, or using two transducers. By using a single transducer two foci were created and fluorescence images were captured using digital optical phase conjugation focusing methods. It was seen that using multiple US foci one can achieve fast AO imaging that is an important challenge to overcome because the decorrelation time of tissue is about 1ms. In another study, Young's Modulus

of the medium was found by forming beat frequency using two US frequencies. By changing the frequencies, they found the resonance of the region which is related to the Young's Modulus of the material. Moreover, the modulation SNR at resonance frequency was higher than the non-resonance frequencies. Furthermore, the nonzero average phase variations at different beat US modulation frequencies can be used to determine localized index of refraction within the medium. Using two different transducers (shown in Figure 3 (a)) a beat frequency could also be achieved and by using this the light was modulated at the beat frequency of US where the two foci intersected. This method improved the axial resolution by 2.4 times to 1.1 mm [4].

ii) Pressure Contrast

Using US signal at 0.3 and 1.5 MPa pressures emitted 96 μm apart and a PRC detection system, Lai et. al. found that by varying the pressure amplitude different optical output intensities are produced. The ratio of intensities that they formulated as pressure contrast signal (PCS) was independent of the characteristics of the detection system and the amount of modulation light detected. Moreover, PCS can be related to the mean free path of the light and therefore it could provide the scattering coefficient of the media [4].

iii) Second-harmonic generation

The US second harmonic in AO imaging was employed by creating a US pulse sequence followed by its inversion. This sequence was repeated at a phase shift of $\pi/2$. The phase-modulated speckle pattern was acquired by applying optical pulses in the medium. A sufficient axial and lateral resolution improvement was seen due to ultrasound pulses. Furthermore, a second harmonic lock-in technique was developed which improved the lateral resolution, but the SNR deteriorated and further development of multipixel lock-in parallel speckle detection technique optimized the SNR [4].

iv) Planar ultrasound

US plane waves are used to modulate light and acquire AO signal which is then used for implementing filtered back-projection to get the reconstructed image. This method achieved high imaging speed, but the reconstructed image was distorted in the lateral resolution which was further corrected by using a second transducer perpendicular to the first [4].

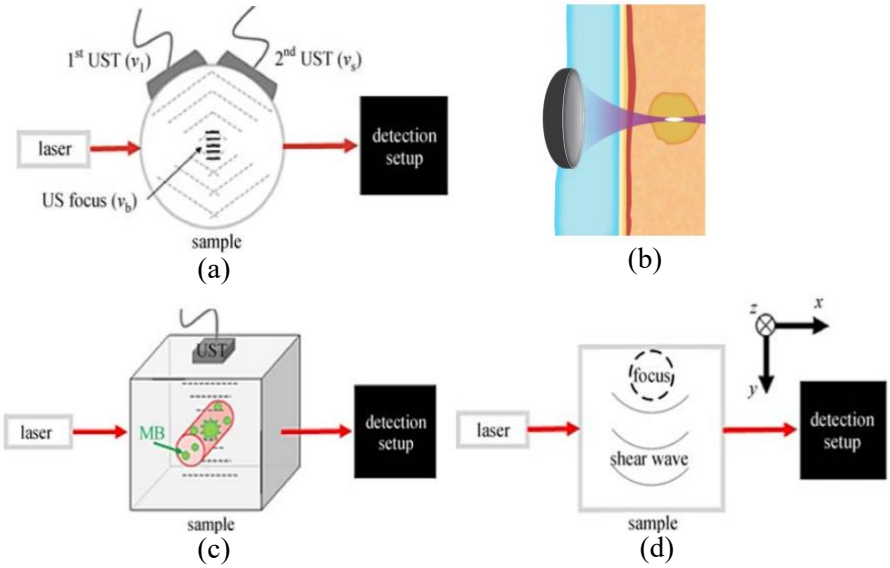

Figure 3 (a) Two transducer US configuration, (b) HIFU setup, (c) Microbubble based AO setup, and (d) Shear wave US [4]. Reprinted by permission from Springer Nature.

v) HIFU monitoring

HIFU is used for tumor ablation (shown in Figure 3 (b)) and treatment but due to the heterogeneous nature of tissues it is difficult to estimate HIFU intensities. Therefore, AO imaging could be used for real-time monitoring of the US-induced tumor ablation. Li et. al. used AO imaging with PRC-based detection and the US to modulate the light signal and provide the lesion formation. They found out that as HIFU was applied the AO signals decreased and the change in normalized signal was proportional to the lesion size regardless of the US exposure parameter [4].

vi) Microbubble usage in AO

They are commonly used to improve contrast and in AO they are used to enhance the spatial resolution that is done by destroying the microbubble by US that creates a different optical field compared to the unmodulated signal (shown in Figure 3 (c)). The difference between the two signals was phase conjugated back into the sample. Using a single microbubble, they achieved a 2 μm resolution and with many microbubbles, the resolution reached half the size of the US focus. This technique was called time-reversed ultrasound microbubble encoded (TRUME) optical focusing. The peak-intensity to background ratio of TRUME was about 510 which was much higher than time-reversed ultrasound encoded (TRUE) optical focusing system (~2). Contrast in AO imaging was improved by combining microbubble and laser speckle contrast detection setup and the difference between the two images was obtained and phase conjugated back into the sample. With a single microbubble ~2 μm resolution was obtained. Moreover, when many microbubbles were used the resolution improved to half the size of US focus [4], [47].

vii) Acoustic radiation force-based AO

ARF is the unidirectional force that is generated within the medium exposed by US. This generated force causes greater tissue displacement in a few micrometres compared to nanometre displacement by US- and this increases modulation depth of light waves as shown in Figure 3 (d). ARF causes shear waves that move perpendicular to US propagation. Liu et. al. minimized the effect of shear waves by reducing the exposure time of the detector and improving the contrast and spatial resolution. Furthermore, using ARF with AO can also be used to estimate the elasticity and viscosity of the material deep inside the tissue (1.2 cm). Liu et. al. also developed models to track shear wave propagation with laser speckle contrast analysis. They found out that as the shear wave passes through the optical focus more light is modulated in that region and also observed the increase in contrast as the shear wave amplitude increased. Later, Cheng et. al. build ARF system and created a combined shear-wave laser speckle contrast analysis (SW-LASCA) and ARF-assisted

US-modulated optical tomography system. With this system they were able to measure absorption information at centimeter depths and measure the elasticity of tissue phantoms [4].

viii) Coded ultrasound transmission

A coded sequence of coded-transmission ultrasound (CT-US) pulse is transmitted into the image object. As the coded pulse change, the modulated signal also changes and thus gives a set of multiplexed measurements. This provides the details of individual contributions from each region in the image medium. The authors used 79 cycles of CTUS which resulted in four-fold increase of SNR in contrast to single-cycle AO imaging [48].

ix) Ultrasound field-perturbation (UFP) optical focusing

In a TRUE optical focusing system a first-order US-modulated light is phase inverted to focus back into the medium whereas, in UFP, zeroth-order light that is not US modulated but in contact of US field the light has field perturbation which can be leveraged to guide light in the scattering medium. The UFP method works by detecting and time-reversing the differential field of the frequency-unshifted photons when the US is alternatively ON and OFF, and thereafter focusing this differential signal back where the field perturbation occurs inside the scattering medium. This technique was demonstrated to be superior to conventional TRUE optical focusing. Furthermore, this technique could also be developed into single-shot or double-shot realization which is desirable for the implementation of high-speed wavefront shaping [49].

2.2.2.2 **Detector technology for tagged photons**

i) Point detectors

The first detection technique (shown in Figure 4 (a)) for US modulated light was done by using point detectors such as photodiodes and photo-multiplier tubes (PMTs). These detectors only detect intensity modulation of a single speckle. The advantage of point detectors is that they are very fast, easy and

have low cost, and detects speckle before it decorrelates (<0.5 ms). The disadvantage of point detectors is the poor SNR due to extremely weak intensity of single speckle [2].

ii) Parallel detectors

In these detectors, a CCD or CMOS camera is used to simultaneously detect N speckles grains. This detection technique improves SNR by sqrt(N) without compromising modulation depth. However, due to limitations in the acquisition speed of cameras prevent them from directly recording the AO modulations. To circumvent this problem the speckle pattern is imaged at four different acquisitions with phase delays of 0°, 90°, 180°, and 270° are acquired, and by computing linear combinations of the four images, the amplitude and phase can be found at each pixel location. But the time required to get four images is very large in comparison to tissue decorrelation time and so, this detection method is normally post-processed and not demonstrated in real-time. The detectors were utilized in measuring speckle contrast and one of the methods compared the speckle pattern with and without US perturbation. Moreover, speckle patterns were used to analyse the interactions

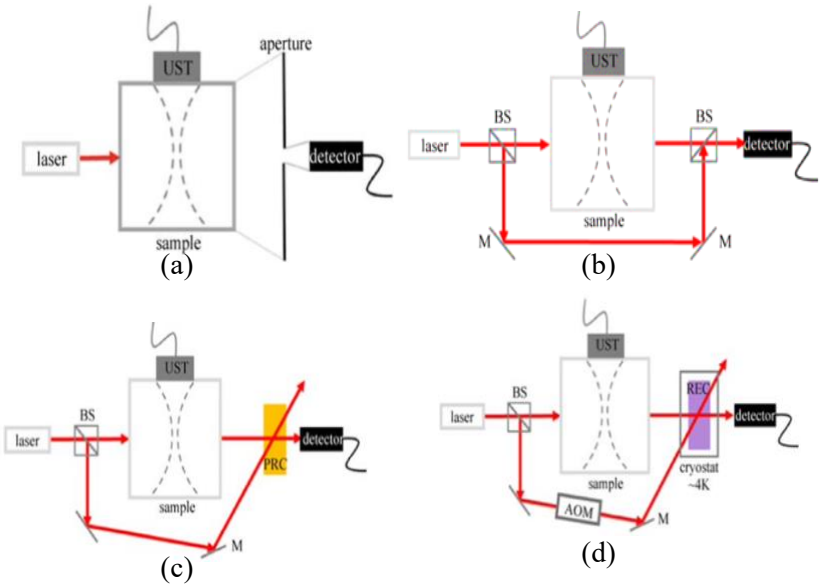

Figure (4) (a) Point detector, (b) HDH detector, (c) PRC detector, and (d) SRH detector [4]. Reprinted by permission from Springer Nature.

of high-intensity nanosecond laser pulses with tissue phantoms, and theoretically, the fraction of tagged light could be calculated from the speckle patterns and from speckle contrast images. The parallel speckle detection is an efficient technique, but this detection method is sensitive to speckle decorrelation time which lowers the SNR [4].

iii) Heterodyne digital holography (HDH)

To solve the problem of parallel detectors, interferometric techniques were developed for AO. In heterodyne digital holography Figure 4 (b) a source laser is made to split into two i.e., one beam travels to the sample while the other acts as a reference beam (local oscillator). The reference beam is either made frequency shifted by AO modulators to match the frequency of modulated photons or has the same frequency as the input signal. If the reference and the modulated signal have similar frequency, then they will form low beat frequency and this interference between the beams is easily detected. But the interference with the unmodulated beam results in a high-frequency beat signal that can be averaged out during the camera exposure time. The strength of the detected signal depends on the reference and transmitted signal [41]. The sensitivity of this technique is limited to the shot noise of the reference light and limitations to the acquisition time of the camera. The development of the Fourier transform acousto-optic imaging (FT-AOI) system with interferometric detection has the SNR significantly. Recently, off-axis holographic detection-based FT-AOI system was developed which used plane US waves with long-duration pulses to perform in-depth imaging inside multiple scattering sample [50].

iv) Photo-refractive crystals (PRC)

The PRC has a refractive index that depends on the light intensity and when the reference and the modulated beam interfere in the PRC there is a slight change of refractive index which causes diffraction (photorefractive effect) of the reference beam inside the crystal as shown in Figure 4 (c). The reference beam after diffraction has the same wavefront and direction as the signal beam

and this is commonly known as two-wave mixing. The photorefractive effect selects optical frequencies from signal which are very close to the reference beam. The PRC can also be used in a four-wave mixing technique which can focus light deep into the tissue (phase conjugation). Various methods of phase conjugation using PRC are developed.

The advantage of this technique is the large etendue and SNR compared to the most CCDs detection scheme and high imaging depth. The disadvantages of this detection can be high background light due to scattering of a strong reference signal and the response time (~ 100 ms) is too slow for in-vivo application. There has been the development of various photorefractive crystals have taken place to increase the imaging speed. For example, GaAs at 1064 nm has 0.3 to 100 ms response time, 1% tellurium-doped tin thiohypodiphosphate ($Sn_6P_2S_6$:Te) crystals has a response time of < 10 ms, a neodymium-doped vandate (ND:YVO_4) PRC has 50 μs response time. Changes in speckle pattern slower than this response time are not recorded, making the detection insensitive for slow speckle decorrelation. The imaging depth of 9.4 cm in phantoms was demonstrated by Lai et. al. with optical inclusion at the half-way depth. They used the transmission setup with $Bi_{12}SiO_{20}$ (BSO) PRC that has a response time of 150 ms at 532 nm. Furthermore, PRC based detection system is used for TRUE optical focusing setups, and to improve the spatial resolution of the TRUE system, time-reversal of variance encoded (TROVE) was developed. Also, another method iterative TRUE (i-TRUE) light focusing was developed and it increased the spatial resolution to ~2 and ~3 fold in the axial and lateral direction, respectively [4], [41].

v) Spectral hole burning

SHB crystal is a rare earth ion-doped optical absorber and has a two-level atomic energy level structure in which specific atoms have different transition wavelength. When the high-powered AO modulated laser beam is incident on cryogenically cooled SHB crystal then the crystal burns and only the ions which are sensitive for this specific frequency are excited from the ground

state. This causes the crystal to transmit the frequency transparently whereas absorbing the frequency of untagged photons (shown in Figure 4 (d)). The major advantage of this technique is high imaging depth which can be achieved with better SNR. The major disadvantage of this technique is the cryogenic cooling (~4 K) of the crystal. Using SHB with a PR:YSO crystal and slow light Zhang et. al. saw 9 cm into the tissue. They reported 30 dB suppression of untagged background [4], [41].

2.2.3 Applications of AO

2.2.3.1 **Image Reconstruction using AO**

AO tomography can provide the absorption and scattering mapping of the tissue. Some of the groups have developed algorithms to map these parameters. Powell et. al [3] used a modified forward diffusion model with a linear reconstruction algorithm to obtain the absorption coefficient. Also, they developed a non-linear reconstruction model to get both scattering and absorption coefficients for 2D images. They also developed an adjoint-assisted gradient-based image reconstruction method to obtain both the coefficients in 2D and 3D. Bal et. al. developed an inverse problem diffusion equation-based reconstruction algorithm to obtain absorption and diffusion coefficient from incoherent measurement of modulated light. Furthermore, they developed solution to the hybrid inverse source problem and reconstruction algorithm to obtain density of luminescent source in bioluminescence acousto-optic tomography. Ammari et. al. [4] constructed non-linear coupled system -using spherical Radon transform inversion and the diffusion model- and solved iteratively to reconstruct the absorption coefficient. Huyung et. al. [4] reconstructed pulsed AO signals along the US axis using maximum likelihood algorithm. By using coupled system equation of diffusion approximation and autocorrelation function Allmaras et al. [4] developed an iteration-based reconstruction algorithm and achieved good stability and resolution in absorption coefficient mapping. Also, Bratchernia et. al. [4] modified diffusion approximation and only considered variation in absorption in their model-based inversion reconstruction method. They were able to determine the location and absorption of embedded absorbers in the phantom.

Verma et. al. [4] moved a step further by developing a reconstruction algorithm to obtain Young's Modulus of the tissue. Their method used diffusion approximation for forward model and solved the inverse problem using the Gauss-Newton method. Backprojection algorithm like CT, X-ray was also developed in AO tomography by Wang et. al. [4]. Chung et al. obtained the scattering and absorption coefficient by reconstruction with Lipschitz stability by means of algebraic inversion formulas [51]. Also, in another work they reconstructed absorption coefficient from the boundary measurement of a single illumination [52]. Recently, Chung et al. analysed the Knudsen (K_n) number's role on stability in AO image reconstruction. They discovered that when K_n decreases to zero, photon scatter more frequently and causes information loss which results in bad reconstruction. To diminish this problem, they posited that the laser beam must be highly concentrated [53].

2.2.3.2 **AO with Photoacoustic tomography (AO-PAT)**

PAT and AO have both complemented each other. In one of the studies, PAT-guided ultrasound wavefront shaping was done to improve AO imaging. On the other hand, AO imaging was utilized to reduce fluence variations in PAT signals. Furthermore, PAT and AO were combined to measure oxygenation in blood samples [19].

2.2.3.3 **Blood Glucose detection by AO**

In this study, the ultrasound optical sensing system (UOS) for non-invasive glucose measurement that uses a 1645 nm laser light and a single element focused transducer with 1 MHz central frequency was presented. The transmittance and absorbance relative to 500-1900 nm wavelength were measured in a vessel-mimicking phantom for different concentrations of glucose solution. Due to higher modulation depth in comparison to the continuous US, the burst mode US was used in this study. In phantom experiments, the measurements were done at the depth of 10 mm depth and the accuracy of the predicted glucose concentration from the US modulated signal was 26.6% mean absolute relative difference

(MARD) which is considered as good in comparison to FDA guidance for the MARD of a glucose meter is within 20% [54].

2.2.3.4 **AO with Diffuse correlation spectroscopy**

AO-DCS combines the sensitivity of DCS to blood flow with ultrasound resolution. This technique could improve the spatial resolution of the optical signal based on the knowledge of US insonified area. This technique is useful in quantifying relative flow differences at different depths in tissue and quantification of fluid flow in a capillary tube embedded in a scattering phantom in the transmission geometry [19].

2.2.4 AO Commercial devices

2.2.4.1 **c-Flow**

This device is developed by Ornim Medical Ltd and is FDA and CE approved. Non-invasive AO monitoring of cerebral oxygen saturation is possible with this device. It consists of AO monitor that emits coherent, near-infrared light, at three wavelengths between 780-830 nm through an optical fiber and collects the backscattered light through an optical fiber to the avalanche photodiode. Ultrasound having a central frequency of 1 MHz was applied on the head and it penetrated the skull with relatively low attenuation. The cross-correlation of the detected signals is analysed, and their spatial decay enables the extraction of the effective attenuation coefficient of the tissue, at selective depths. The extraction of wavelength-specific absorption by oxygenated and deoxygenated haemoglobin is possible and on further analysis, the regional oxygen saturation of blood in the microvasculature of the brain can be obtained. This device can measure 1 cm deep below the skin and provides applicability of using AO signal to measure cerebral oxygen saturation in traumatic brain injury patients at risk of cerebral ischemia. Furthermore, the device also provides cerebral blood flow information and monitors tissue microcirculation [4], [55].

3 Methods and Materials

The AO phenomenon consists of two parts: the acoustics and the optics, and to perform modelling and simulation we need to consider these two effects separately. In this section we will develop the FUS simulation model to simulate US in human brain and the MC model for light propagation. Moreover, we will then develop a single AO MC model to simulate the whole AO effect in brain tissue.

3.1 Focused-Ultrasound Modelling

The FUS modelling and simulation is done using open-source k-Wave MATLAB toolbox [56]. The k-Wave toolbox is especially designed for the time-domain simulation of US waves in 1D, 2D, and 3D and has a variety of functions to simulate the linear US, non-linear US, PAT reconstruction, and FUS heating. In k-Wave the propagation of US wave in a heterogeneous medium can be described by the system of coupled first-order partial differential equations given as,

$$\frac{\partial \mathbf{u}}{\partial t} = -\frac{1}{\rho_0}\nabla p\,, \tag{1}$$

$$\frac{\partial p}{\partial t} = -\rho_0 \nabla \cdot \mathbf{u} - \mathbf{u} \cdot \nabla \rho_0\,, \tag{2}$$

$$p = c_0^2(\rho + \mathbf{d} \cdot \nabla \rho_0 - L\rho)\,, \tag{3}$$

The above equations are momentum conservation, mass conservation, and pressure-density relation, respectively. The terms $\mathbf{u}$ is the acoustic particle velocity, p is the acoustic pressure, ρ is the acoustic density, ρ_0 is equilibrium density, c_0 is the isentropic sound speed, $\mathbf{d}$ is the acoustic particle displacement, and L is a linear integro-differential operator that accounts dispersion and acoustic absorption in the medium which follows frequency power law $\alpha = \alpha_0 \omega^y$ where, α is the absorption coefficient, α_0 is power law prefactor and ω is the angular frequency, and y is the power law exponent. In most soft biological tissues y is ≈ 1. In k-Wave, the above partial differential equation is solved using discrete k-space pseudospectral method (k-space method) where spatial gradients are calculated using Fourier-collocation method and conventional finite difference method is used to calculate temporal gradients. However, the grid-based technique used to solve the collocation method does not accurately represent the US source distribution (especially when the source is curved) as the source grids points do not coincide with it.

This causes staircasing error near the source surface and results in erroneous acoustic field distribution which provides inaccurate results in the case of FUS therapy. To avoid this grid-based error we used the kWaveArray class [57] which applies the discrete, band-limiting convolution operator to the continuous distribution of source and can accurately describe the acoustic pressure distribution in therapeutic US settings. It supports arbitrary shaped sources which are not constrained to the grid points and can be placed anywhere inside the computational grid.

3.2 Numerical Implementation of FUS in k-Wave

The FUS implementation in k-Wave was done using single element bowel-shaped focused transducer with 50 mm diameter and a focal length of 40 mm. We considered two central frequencies 0.5 MHz and 0.9 MHz of the custom build transducer (f-number = 0.9) to simulate the pressure distribution in SLB medium and FLB medium that consists

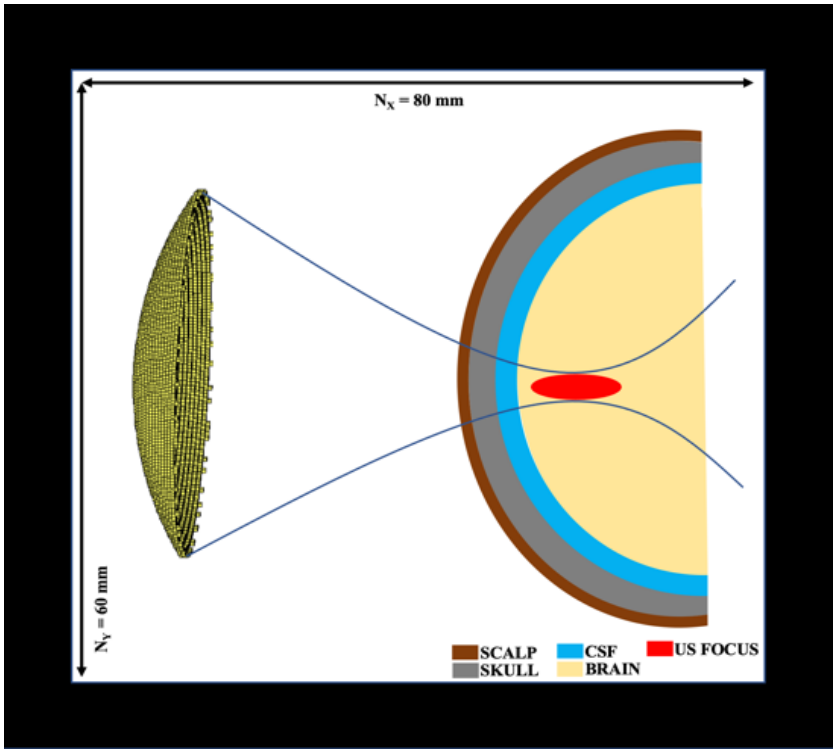

Figure 5 The computational domain of the simulation.

of scalp, skull, CSF, and brain. Our aim through US simulations was to investigate the focal pressure, the displacement of focus point in presence of skull, and US heating at the focal point. In our all simulations, the focal pressure was about 0.5 MPa as several studies

[58] has shown that a pressure of 0.2-0.7 MPa is optimal for BBB opening. The computational grid size was taken as 124 x 124 x 164 with Δx, Δy, and Δz all equal to 0.5 mm and width of the perfectly matched layer (PML) was twenty grid points. Inside the computational domain as shown in Figure 5, FLB medium is modelled as concentric semicircles and the background medium is water. The distance between the transducer and the brain is 28 mm while the centre of the FLB medium is 13 mm away from the midpoint of the computational domain. The ultrasound focus was positioned at 10 mm from the CSF layer and the background temperature was about 22 ℃. Furthermore, the exposure time for the ultrasound was 2379 steps with a temporal resolution (Δt) of 18.5 ns and for the stability the Courant–Friedrichs–Lewy (CFL) number $\left(\frac{v_a \Delta t}{\Delta x}\right)$ was 0.1 where v_a is the speed of US in the skull medium. Figure 6 shows excellent fit between the transducer field in the axial direction simulated in k-Wave and O'Neill's analytical model [59].

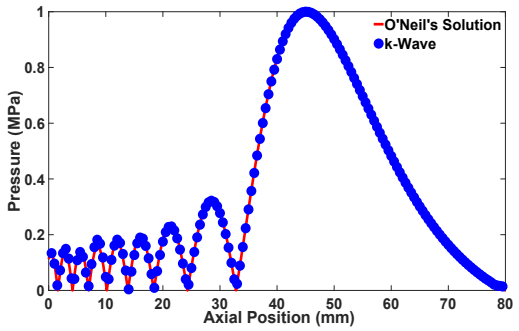

Figure 6 The pressure field in axial direction from k-Wave (blue) and O'Neil's Model (red).

Table 1. US Parameters

	v_a	ρ	α_0	y	L
Water	1500	1000	0.002	1.1	
Scalp	1537	1116	0.85	1.1	3
Skull	2652	1796	4.11	1.1	7
CSF	1500	1000	0.002	1.1	3
Brain	1500	1000	0.10	1.1	25

v_a= ultrasound velocity (m/sec)

ρ = density (kg/m^3)

α_0= power law prefactor (dB/(MHz)^y cm)

y = power law exponent

L = thickness (mm)

3.3 The Monte Carlo Light Propagation Model

The flow of optical energy in turbid media can be described by radiative transport equation (RTE) which is based on energy conservation law [60]. The solution to RTE exists for simple geometries and is given by applying diffusion approximation which

assumes that photons are diffusing in the medium after they have travelled the distance known as transport mean free path (l_{tr} = $(1/\mu_s')$ [61]. However, the diffusion approximation is valid only for distances greater than one transport mean free path and for mediums with low absorption coefficient. Another approach to solve the RTE equation is through MC method which is a stochastic method. The MC method is a tool to solve problems using random numbers and are very useful where analytical solution is very difficult to get. In tissue medium the MC method simulates the "random walk" photons make while propagating through the tissue, which is calculated by statistically sampling the probability distributions to get step size and scattering direction [62]. Moreover, after enough photons the MC method gives accurate solution to RTE. However, a large amount of computation time is required to get the accuracy and that is why several parallelization algorithms are developed to simulate hundreds or thousands of photons simultaneously. The MCX is one of the open-source algorithms that is based on GPU computing and can simulate billions of photons simultaneously [63]. The events a photon experiences while travelling in the tissue medium is shown in the flowchart Figure 7 and below is the detailed explanation of the MC flowchart. Initially the photon is launched from a unity pencil beam that has a specific location (x, y, z) and a direction $(\widehat{\Omega_x}, \widehat{\Omega_y}, \widehat{\Omega_z})$. Each photon moving out from the source has a unity weight (energy) and the specular reflection coefficient is calculated at this point if there is a refractive-index-mismatched interface between the tissue and the ambient medium. As some of the photons reflected due to specular reflection some weight of the photon is reduced as W = W – R_{sp} , where W is weight of the photon and R_{sp} is the specular reflection coefficient. Once the photon is launched, the step (s) photon will take to move forward is calculated from a randomly chosen value from exponential distribution, and is calculated by [62]:

$$s = -\frac{\ln \zeta}{\mu_t}, \tag{4}$$

where ζ is the random number distributed between 0 and 1, μ_t is the interaction coefficient defined as $\mu_t = \mu_s + \mu_a$, where μ_s is the scattering coefficient and μ_a is the absorption coefficient. The photon's movement that is its x, y, and z positions are updated in cartesian coordinate system. Then we will test if this step size (s) is less than the distance between current photon position and boundary of the medium.

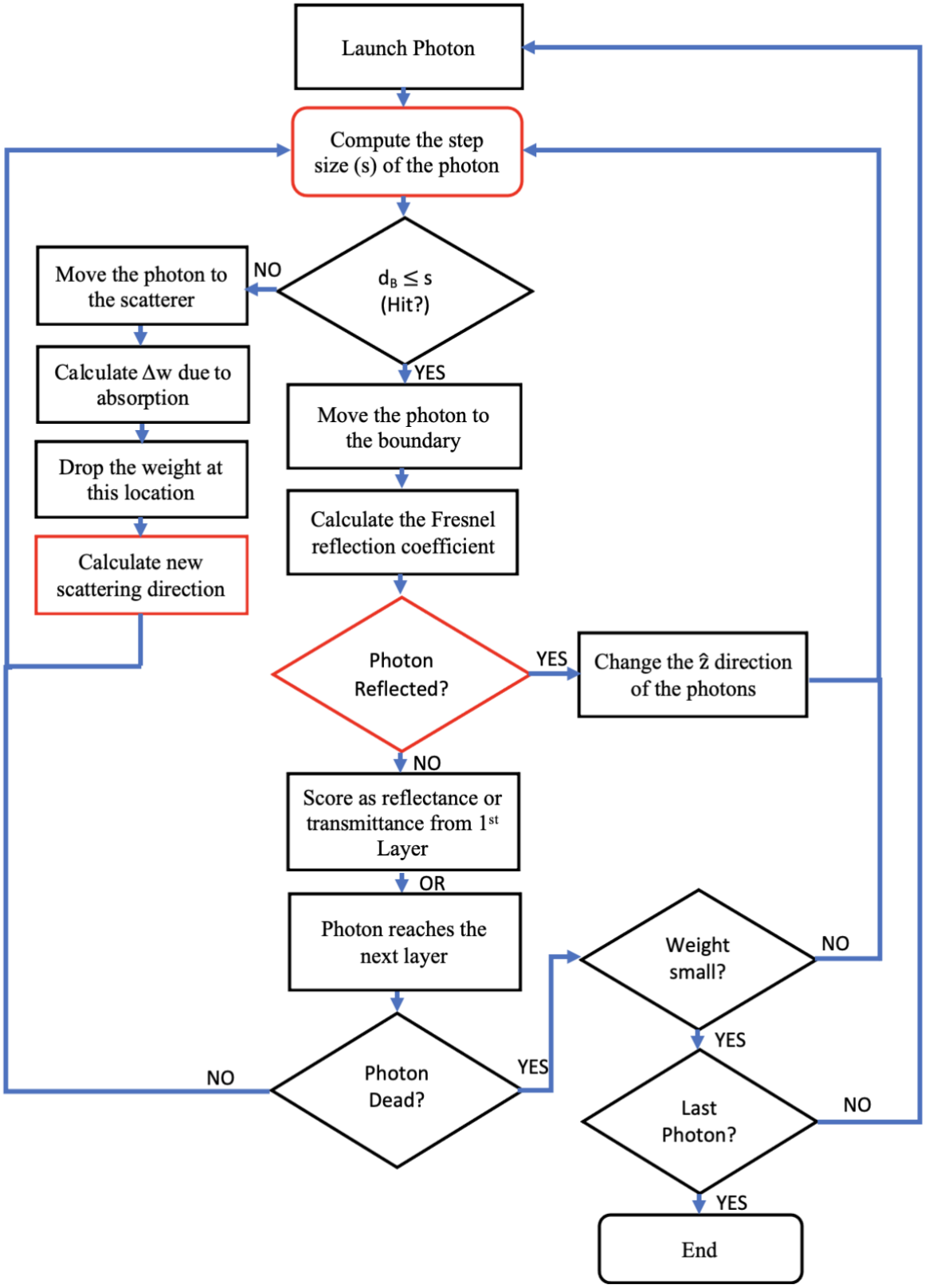

Figure 7 Flowchart of a single photon in a Monte Carlo light transport model. The red boxes indicate the random number generation from a probability distribution.

If this is false, then move the photon and calculate the amount of weight Δw to be dropped at this location [62]:

$$\Delta w = W * \frac{\mu_a}{\mu_t}, \tag{5}$$

the current photon's weight is decreased as W = W - Δw and the Δw is added to the current voxel of the tissue medium. Moreover, after dropping the weight the photon will experience scattering and its direction is updated. In MC direction vector is represented in spherical coordinate system (r, θ, φ). The cosine of the polar deflection angle, $\cos\theta$, is calculated using Henyey-Greenstein phase function [62],

$$\cos\theta = \begin{cases} \frac{1}{2g}\left[1 + g^2 - \left(\frac{1-g^2}{1-g+2g\zeta}\right)^2\right] & \text{if } g \neq 0 \\ 2\zeta - 1 & \text{if } g = 0. \end{cases} \tag{6}$$

In the above equation g is the anisotropy and has values range from -1 to 1 representing complete backward scattering and complete forward scattering, respectively. The azimuthal deflection angle (φ), is a uniformly distributed over 0 to 2π, given as,

$$\varphi = 2\pi\zeta \tag{7}$$

Once the deflection angles are in hand we can calculate the updated direction of the photons as,

$$\begin{aligned} \hat{\Omega}_x' &= \frac{\sin\theta(\hat{\Omega}_x \hat{\Omega}_z \cos\varphi - \hat{\Omega}_y \sin\varphi)}{\sqrt{1-\hat{\Omega}_z^2}} + \hat{\Omega}_x \cos\theta, \\ \hat{\Omega}_y' &= \frac{\sin\theta(\hat{\Omega}_y \hat{\Omega}_z \cos\varphi + \hat{\Omega}_x \sin\varphi)}{\sqrt{1-\hat{\Omega}_z^2}} + \hat{\Omega}_y \cos\theta, \\ \hat{\Omega}_z' &= -\sqrt{1-\hat{\Omega}_z^2}\sin\theta\cos\varphi + \hat{\Omega}_z \cos\theta. \end{aligned} \tag{8}$$

In Equation 8 the $(\hat{\Omega}_x', \hat{\Omega}_y', \hat{\Omega}_z')$ is the updated direction of the photon.

However, if the step size is greater than the distance between current photon position and the boundary. Then the photon is moved to the boundary and Fresnel reflection coefficient $R(\phi_i)$ is calculated [62],

$$R(\phi_i) = \frac{1}{2}\left[\frac{\sin^2(\phi_i - \phi_t)}{\sin^2(\phi_i + \phi_t)} + \frac{\tan^2(\phi_i - \phi_t)}{\tan^2(\phi_i + \phi_t)}\right], \quad (9)$$

where $\phi_i = \cos^{-1}(|\widehat{\Omega}_z|)$ is the angle of incidence on the boundary and ϕ_t is the angle of transmission which is calculated by Snell's law. After calculating $R(\phi_i)$, a random number is generated to determine whether the photon is internally reflected or transmitted if $\zeta \leq R(\phi_i)$ then the photon is internally reflected and, in this condition, the $\widehat{\Omega}_z$ direction of the photon is changed. If $\zeta > R(\phi_i)$ then the photon transmits in the next medium or exits outside the tissue medium. If the exiting photon is incident upon a detector, its final weight, and partial path length in each tissue medium are saved. Furthermore, the photon once exited will be dead and a new photon will be simulated. This recursive process will complete only after all the photons are simulated.

(a)

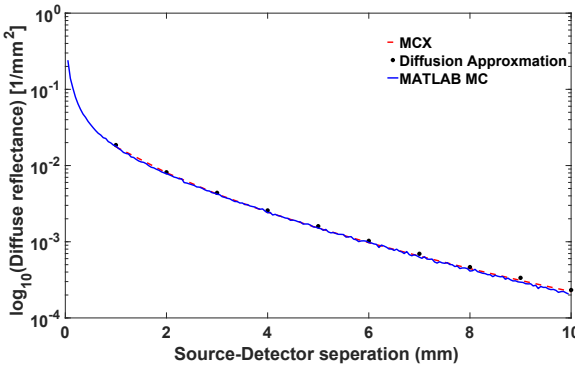

(b)

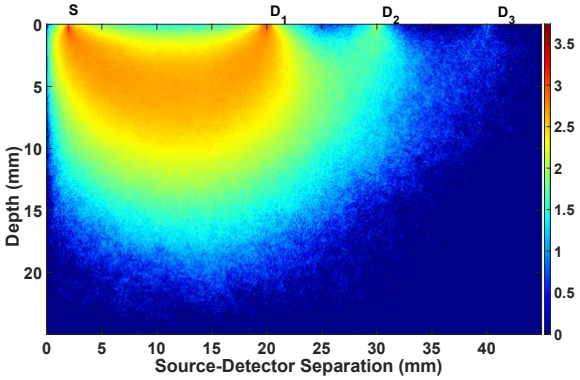

Table 2. Optical properties

	μ_a	μ_s	g	n
Scalp	0.037	9.5	0.8	1.37
Skull	0.028	27	0.9	1.43
CSF	0.004	0.016	0.9	1.33
Brain	0.035	8.5	0.9	1.37

n = refractive index

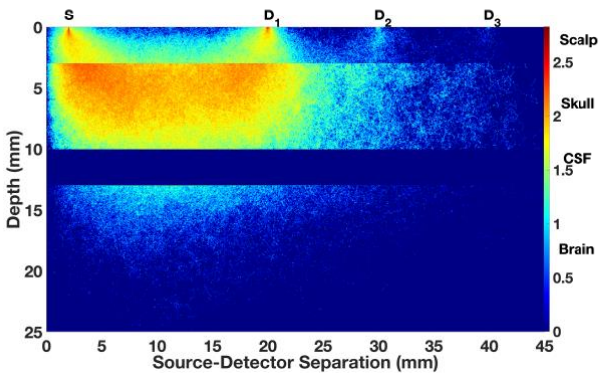

(c)

Figure 8 (a) The validation of our MC model with MCX and Diffusion approximation, (b) Photon trajectories in semi-infinite SLB medium, and (c) Photon trajectories in FLB medium and the color bar shows frequent paths photons take while traversing to the detectors.

In our study I developed the MC program on MATLAB using the same principles described above. Like the US simulation, the photons were simulated in two semi-infinite mediums, one representing the SLB and other is a FLB medium. The Table 2 shows the optical properties of the medium at 850 nm wavelength of light [64]. The internal reflection from the boundary was considered as all-or-none event, this means that no partial reflection or refraction was considered for a photon. The validation of our MC model (shown in Figure 8 (a)) was done with the diffusion approximation equation and MCX's diffuse reflectance curve. 10 million photons were simulated in 60x60x60 grid points semi-infinite brain medium with Δx, Δy, and Δz as 0.5 mm. The diffuse reflectance was calculated by placing 100 detectors (r = 0.05 mm) on the topmost layer of the medium. All the applications of biomedical optics in the head where the light source is involved, the source and detectors are at the same side and the efficient placement of the detectors is the key. The source-detector separation determines the depth the photon will travel inside the medium before reaching the detector and increasing the source-detector separation we can probe deeper inside the tissue. The Figure 8 (b) and (c) shows the photon trajectories reaching the detectors D_1, D_2, D_3 placed at 20 mm, 30 mm, and 40 mm, respectively for both the mediums. We can observe that as the detector position is increasing the photons reaching the detectors D_2 and D_3 have travelled deep inside the tissue before reaching the detectors.

3.4 The Acousto-Optics Modelling

The AO effect modulates the phase of the light and as the light is detected it forms speckle patterns. The two mechanisms: refractive index change and scatterer displacement, contribute to the total phase change of a photon. This section introduces the AO equations relevant for the calculation of magnitude of the total phase change for each photon. While deriving the equation it was assumed that- the mean free path of a photon is much greater than the optical wavelength, the ultrasound induced displacement of scatterers is much less compared to the optical wavelength and ultrasound induced refractive index change is very small and is linearly proportional to pressure amplitude. The last two assumption place a limit to the US pressure to $P_0 \leq 10^5$ Pa in biological tissue for valid result [65], [66]. Moreover, we also assume that in biological tissues at length greater than l_{tr}, the

monochromatic US field is uniform and we can locally approximate the US pressure as $P(\mathbf{r},t) = P_0\cos(\omega_a t - \mathbf{k}_a \cdot \mathbf{r} + \phi)$, where $\mathbf{k}_a = k_a\ \widehat{\Omega}_a$ is the ultrasound wave vector and P_0 is the pressure amplitude, ω_a is the acoustic angular frequency, ϕ is the local initial phase, and $\widehat{\Omega}_a$ denote the direction unit vector of US propagation. With locally available US pressure we can calculate the phase change experienced by the light.

3.4.1 Phase change due to refractive index perturbation

The propagating US pressure alters the refractive index of the medium. This change in the refractive index is given by [66],

$$\Delta n(\mathbf{r},t) = n_0 \frac{\partial n}{\partial p} p(\mathbf{r},t), \tag{9}$$

where $\Delta n(\mathbf{r},t)$ = change in the refractive index, n_0 = initial refractive index, η (elasto-optic coefficient) $= \rho\ v_a^2 \frac{\partial n}{\partial p}$, ρ = density of the medium, v_a= speed of acoustic wave. The change of refractive index between the scatterers causes the phase change of photon as they scatter from one scatterer to another. Assuming the plane electromagnetic wave with k_0 (optical wave number) propagating between two scatterers positioned at $\mathbf{r}_{i-1}$ and $\mathbf{r}_i$ the phase change due to refractive index is given by,

$$\phi_{n,i}(\mathbf{r}_{i-1}, \mathbf{r}_i, t) = k_0 n_0 \frac{\partial n}{\partial p} \int_{\mathbf{r}_{i-1}}^{\mathbf{r}_i} p(\mathbf{r}, t)\, d\mathbf{r}, \tag{10}$$

3.4.2 Phase change due to displacement of scatterers

The propagating US pressure also causes the displacement of scatterers ($\boldsymbol{\varrho}_s$) and as the photon interacts with the moving scatterer its path length changes at each scattering event. To avoid the complex interaction of light and background medium, we assume that the background medium movement is in phase with moving scatterer. The expression for displacement of scatterer is [67],

$$\boldsymbol{\varrho}_s(\mathbf{r}, t) = \frac{\widehat{\Omega}_a}{\rho_0 v_a} \int p(\mathbf{r}, t)\, dt, \tag{11}$$

where ρ_0 is the density of the medium, v_a is the speed of US in the medium, and $\widehat{\Omega_a}$ is the propagation direction of US. Given Equation 11 we can calculate the phase variation due to i_{th} scattering event,

$$\phi_{d,j}(\mathbf{r}, t) = \frac{k_0 n_0}{\rho v_a} \widehat{\Omega}_a \cdot (\widehat{\Omega}_{inc} - \widehat{\Omega}_{sc}) \int p(t)\, dt, \tag{12}$$

here in Equation 12, $\widehat{\Omega}_{inc}$ is the incident direction of photon, $\widehat{\Omega}_{sc}$ is the scattered photon direction. We have from Equation 10 and 12 the individual phase modulation expressions from both the mechanisms. Now the ultrasound induced total phase modulation of photon over a single optical path is given by [44],

$$\phi_{us}(t) = \sum_{i=1}^{N} \phi_{n,i}(\mathbf{r}_{i-1}, \mathbf{r}_i, t) + \sum_{j=1}^{N-1} \phi_{d,j}(\mathbf{r}_j, t), \tag{13}$$

where N and (N-1) are the number of free paths and scattering events, respectively. Note that the scatterer displacement and refractive index change are time dependent quantities because they are proportional to US pressure. Therefore, we can express the total phase shift as [68],

$$\phi_{us}(t) = \mathrm{Re}\{|\phi_{us}|(\exp(-i[\omega_a t + \varphi_{us}])\}, \tag{14}$$

where $|\phi_{us}|$ is the magnitude of the total phase when it is expressed in complex exponential and φ_{us} is the phase angle of ϕ_{us}. Thus, the optical wave propagating along the optical path s can be written as the electric field wave,

$$E_s(\mathbf{r}, t) = A_s(\mathbf{r})\exp(-i[\omega_0 t + \phi_{m,s}(\mathbf{r}, t) + \phi_{us,s}(\mathbf{r}, t)]), \tag{15}$$

where $A_s(\mathbf{r})$ is the amplitude, ω_0 is optical frequency, $\phi_{m,s}$ is some random phase due to multiple scattering process for this wave, and $\phi_{us,s}$ is the total AO phase shift in this optical path. The intensity received at the detector will be a randomly fluctuating variable over time and using the Siegert relationship we can get the temporal field autocorrelation function. Moreover, applying the Wiener-Khinchin theorem we can investigate the power spectrum of unmodulated and modulated light by calculating the Fourier transform of the temporal field autocorrelation function, $G(\tau)$ [44],

$$G(\tau) = \left| \int_{-\infty}^{+\infty} E(\mathbf{r}, t)\, E^{*}(\mathbf{r}, t-\tau)\, dt \right|. \quad (16)$$

When evaluating the Equation 16 for all the optical path, the autocorrelation function will be,

$$G_s(\tau) = \sum_s \int_{-\infty}^{+\infty} E_s(\mathbf{r}, t)\, E_s^{*}(\mathbf{r}, t-\tau)\, dt, \quad (17)$$

Neglecting the random phase term $\phi_{m,s}$ and we assume that the system is ergodic and wide-sense stationary, using Equation 15 we can expand the exponential cosine function in Equation 17 to a series of Bessel functions using Jacobi-Angers identity and the final expression is given as [56],

$$G_s(\tau) = A_s^2[J_0^2(|\phi_{us}|) + \sum_{m=1}^{\infty} 2J_m^2(|\phi_{us}|)\cos(m\omega_a\tau)], \quad (18)$$

where J_0 and J_m are the Bessel function of first kind of order zero and m, respectively. Equation 18 is a power spectrum of the zeroth harmonic which is also called DC (unmodulated) component of light at ω_0 and is proportional to $J_0^2(|\phi_{us}|)$. Moreover, the power spectrum of higher harmonics (modulated light) is at multiples of acoustic frequency ($\omega_0 + \omega_a$) and its m_{th} side band is proportional to $2J_m^2(|\phi_{us}|)$.

3.5 Numerical Implementation of AO in Monte Carlo

In this section we will implement the AO equations in our MC model which will be called as AO-MC. The flowchart of AO-MC model is shown in Figure 9, the algorithm for calculating the phase shift of a single photon is very similar to the one used in [10]. The AO modulation process is simulated by considering the local pressure amplitude, the local acoustic phase at that point, and the direction of the acoustic wave. In the first step of AO-MC we will load the pressure amplitude, phase, and direction matrix. Each voxel of the MC computational domain contains four quantities namely, [$P_0\ \widehat{\Omega}_x$, $P_0\ \widehat{\Omega}_y$, $P_0\ \widehat{\Omega}_z$, ϕ_a], where $\widehat{\Omega}_x$ is the direction of the acoustic wave in x-direction.

From the AO theory we can approximate the local pressure in each voxel as [65],

$$p(t) = p_0 \cos(\omega_a t + \phi_a). \quad (19)$$

The simulation of photon propagation in AO-MC is like the MC method but with a slight modification to accumulate the phase shift photon experiences along its path. When the photon moves to a new distance by taking i_{th} step size in tissue layer T, then the phase shift due to refractive index change is accumulated in the current voxel as,

$$\Delta\phi_{n,i,T}(t) = \frac{k_0 n_0 s_{i,T} \eta}{\rho_T v_{a,T}^2} p(t), \tag{20}$$

where T is for tissue layer, $s_{i,T}$ is the i_{th} step size in tissue T, ρ_T and $v_{a,T}$ is the density and US speed of the current tissue layer, respectively. Moreover, by replacing the value of p(t) in Equation 20, we get [65], [67],

$$\Delta\phi_{n,i,T}(t) = p_{n,cos,i,T} \cos(\omega_a t) + p_{n,sin,i,T} \sin(\omega_a t), \tag{21}$$

here in Equation 20:

$$p_{n,cos,i,T} = \frac{k_0 n_0 s_{i,T} \eta}{\rho_T v_{a,T}^2} p_0 \cos(\phi_a),$$

$$p_{n,sin,i,T} = -\frac{k_0 n_0 s_{i,T} \eta}{\rho_T v_{a,T}^2} p_0 \sin(\phi_a). \tag{22}$$

Similarly, at the j_{th} scattering event the phase change due to scatterer displacement is accumulated as [65], [67],

$$\Delta\phi_{d,j,T}(t) = \frac{k_0 n_0}{k_a \rho_T v_{a,T}^2} \hat{\Omega}_a \cdot (\hat{\Omega}_{inc} - \hat{\Omega}_{sc}) \int p(t)\, dt, \tag{23}$$

By putting the p(t) in Equation 20, we arrive the final expression as:

$$\Delta\phi_{d,j,T}(t) = p_{d,cos,j,T} \cos(\omega_a t) + p_{d,sin,j,T} \sin(\omega_a t), \tag{24}$$

where,

$$p_{d,cos,j,T} = \frac{k_0 n_0}{k_a \rho_T v_{a,T}^2} \hat{\Omega}_a \cdot (\hat{\Omega}_{inc} - \hat{\Omega}_{sc})\, p_0 \sin(\phi_a),$$

$$p_{d,sin,j,T} = \frac{k_0 n_0}{k_a \rho_T v_{a,T}^2} \hat{\Omega}_a \cdot (\hat{\Omega}_{inc} - \hat{\Omega}_{sc})\, p_0 \cos(\phi_a). \tag{25}$$

From Equation 21 and 23, we can calculate the total ultrasound induced phase shift, $\phi_{us}(t)$ as,

$$\phi_{us}(t) = \left[\sum_{T=1}^{m}\sum_{i=1}^{n} p_{n,cos,i,T} + \sum_{T=1}^{m}\sum_{j=1}^{n} p_{d,cos,j,T}\right]\cos(\omega_a t) + \left[\sum_{T=1}^{m}\sum_{i=1}^{n} p_{n,sin,i,T} + \sum_{T=1}^{m}\sum_{j=1}^{n} p_{d,cos,j,T}\right]\sin(\omega_a t), \quad (26)$$

and from Equation 14 and 26, the magnitude $|\phi_{us}|$ is calculated as,

$$|\phi_{us}| = \sqrt{A^2 + B^2 + C^2 + D^2} \quad (27)$$

where,

$$A = \sum_{T=1}^{m}\sum_{i=1}^{n} p_{n,cos,i,T}, \qquad C = \sum_{T=1}^{m}\sum_{i=1}^{n} p_{n,sin,i,T}$$
$$B = \sum_{T=1}^{m}\sum_{j=1}^{n} p_{d,cos,j,T}, \qquad D = \sum_{T=1}^{m}\sum_{j=1}^{n} p_{d,sin,j,T}.$$

The phase angle can also be calculated by

$$\angle\phi_{us} = \tan^{-1}\left(\frac{-C-D}{A+B}\right), \quad (28)$$

At each scattering event the $|\phi_{us}|$ is calculated and the unmodulated AO fluence is then accumulated in the n_{th} voxel as $M_{0,n} = J_0^2(|\phi_{us}|)\frac{\Delta w}{\mu_{a,T}}$ and assuming the contribution of higher order terms to be negligible the amount of modulated AO fluence is accumulated in the n_{th} voxel will then be $M_{1,n} = 2J_1^2(|\phi_{us}|)\frac{\Delta w}{\mu_{a,T}}$, where Δw is the current weight of the photon and $\mu_{a,T}$ is the absorption coefficient of current tissue layer where the photon is currently residing. At the end of the simulation the modulation depth (MD) distribution is calculated as [65],

$$MD = \frac{M_{0,n}}{M_{1,n}}. \quad (29)$$

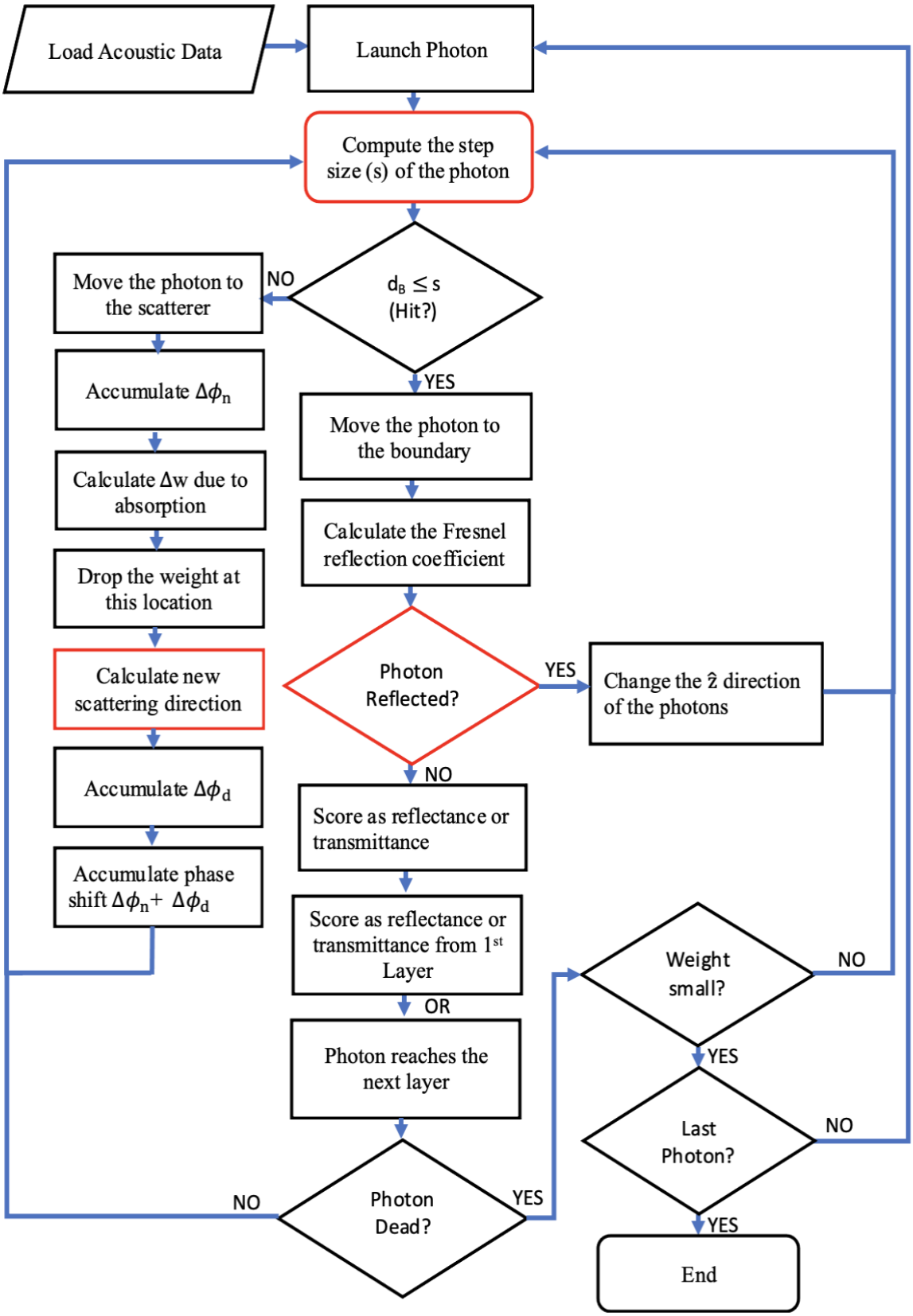

Figure 9 Flowchart of single photon AO-MC model. The red boxes indicate the random number generation from a probability distribution.

3.6 AO-MC simulation procedure

In our AO-MC simulation we simulated the AO effect by the method provided in [65], [67]. The computational grid size was made of 110 points in all directions with a spacing of 0.5 mm and the US transducer was placed at 26 mm in x and y direction. Furthermore, the simulated pressure magnitude, phase, and the average speed 3D matrices data from k-Wave was loaded to the computational domain of AO-MC. The average particle velocity in each direction x, y, and z was used to calculate the direction of the pressure in each voxel. US pressure was normalized to 10 kPa as to fulfil the assumptions made while deriving the AO theory and four simulations were done for 0.5 MHz and 0.9 MHz US frequencies in both the mediums i.e., SLB and FLB medium. Moreover, a total of 100 million photons were simulated and at each scattering event the unmodulated and modulated power spectrum is accumulated to the current voxel of the photon's location. Finally, the total distribution of modulated and unmodulated power spectrum was used in Equation 29 to calculate the MD distribution inside the medium.

All AO-MC codes used for generating results of this thesis can be downloaded from Github (https://github.com/dpksonker).

4 Results

4.1 US simulation

The US simulation results are presented in Figure 10, different configuration of the frequency and pressure amplitude of the transducer was used to get the desired focal pressure of about 0.5 MPa which is the marked pressure for BBB opening.

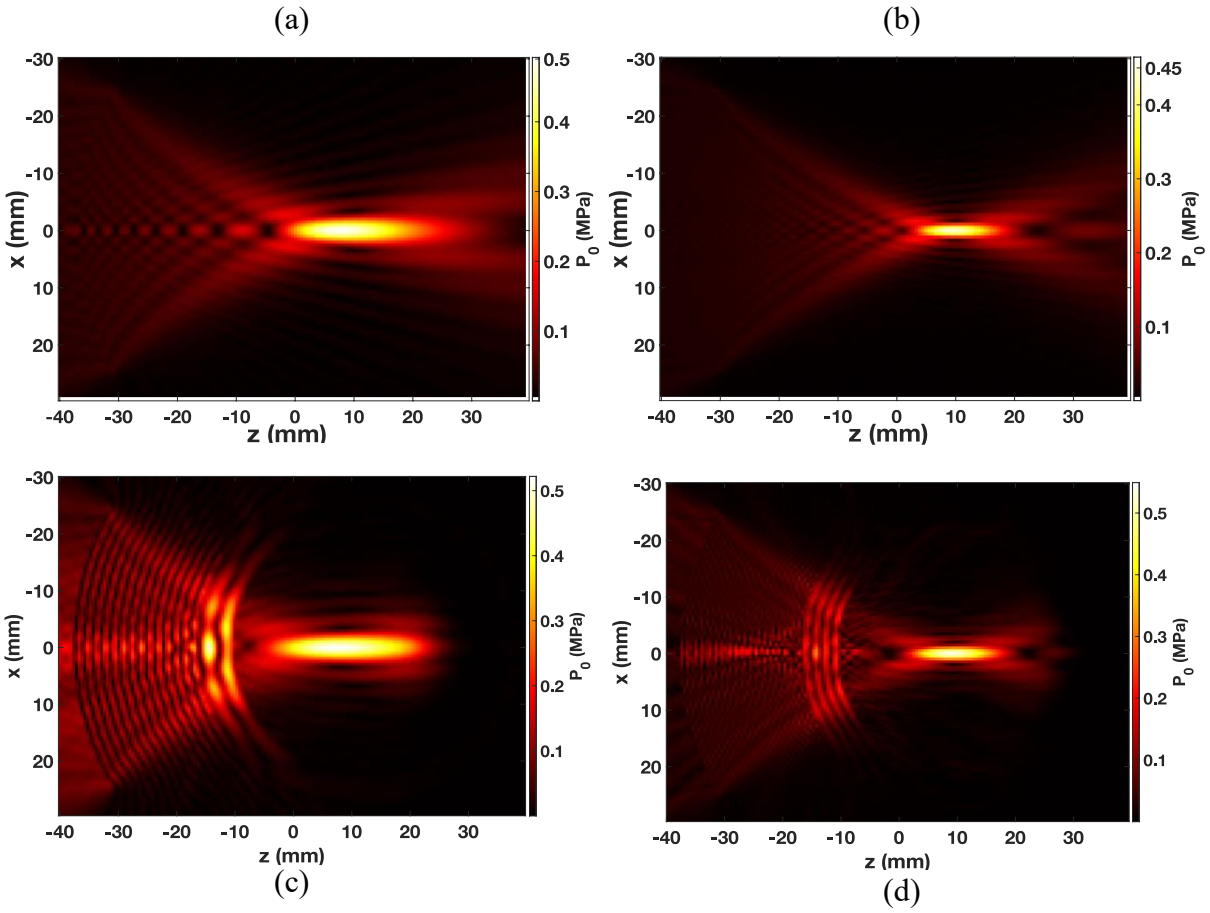

Figure 10 Results from US simulation at different configurations of the medium and frequency: (a) and (b) represent the distribution of pressure in SLB medium at 0.5 MHz and 0.9 MHz and the color bar shows the pressure at focus; (c) and (d) represent the distribution of pressure in FLB medium.

The Mechanical Index (MI) at 0.5 MHz is 0.7 and at 0.9 MHz it is 0.52, both are well below the maximum FDA approved limit [69], i.e., 1.9. Moreover, the temperature increase was 0.002 ℃ at the focus point. Figure 10 (a) and (b) show the pressure profile in SLB medium for 0.5 MHz and 0.9 MHz, respectively. The inverse relationship between US frequency and focal volume is clearly visible. In SLB, at 0.5 MHz the -3 dB focal

length was 16 mm and width were about 3 mm and at 0.9 MHz the -3 dB focal length and width were about 10 mm and 1.5 mm, respectively. We considered the focal point to be at maximum pressure and therefore in simulations the focal depth was about 46 mm from the centre of the transducer. When the FLB medium (having water as the background medium) was placed in the medium, see Figure 10 (c) and (d), the focus was spatially displaced by 0.25 mm and 0.34 mm, respectively towards the transducer. Furthermore, when the skull was introduced in the medium the focal length elongated 4 mm in axial direction and decreased by 0.2 mm in lateral direction for 0.5 MHz. Similarly, for 0.9 MHz the axial elongation was about 0.80 mm and in the lateral direction, it decreased by 0.3 mm. The US transmission coefficient for 0.5 MHz and 0.9 MHz was about 60% and 54%, respectively. Formation of standing waves is visible with US interference pattern before Figure 10 (c) and in the skull Figure 10 (d).

4.2 AO-MC simulation

Figure 11 provides the results of the AO-MC simulation in both the mediums. The first column represents the simulation result from 0.5 MHz US in SLB medium and the second column shows the result for 0.5 MHz US in the FLB medium. The computational domain in each simulation was 50 mm in each direction. Figure 11 (a) and (b) shows the acoustic pressure distribution in SLB and FLB medium, respectively. The centre of the focus point was placed around 20 mm and 28 mm in the z direction for both the mediums. Figure 11 (c) and (d) represents the AO fluence distribution of unmodulated light ($M_{0,n}$) of the power spectrum in SLB and FLB medium, respectively. The source was placed at 10 mm in the x and y direction and the unmodulated light is strong near the source. Also, the extent of unmodulated light near the source is more in SLB than in FLB medium. The AO fluence distribution of the modulated light of the power spectrum is shown in Figure 11 (e) and (f) for both the mediums. We only considered the first harmonic ($M_{1,n}$) of the power spectrum because the contribution from higher order harmonics will be negligible. In the SLB medium, the distribution of the modulated light covers a large area i.e., from near the source to the ultrasound focus area. The area near and at the focus contains high pressure magnitude and so the light will get modulated here strongly however Figure 11 (e) shows high modulation of light near the source also. In the FLB (Figure 11 (f)) the area near the source has high modulation of light due to the presence of scalp and skull as the absorption and reflection of ultrasound from the scalp and skull is large and so most

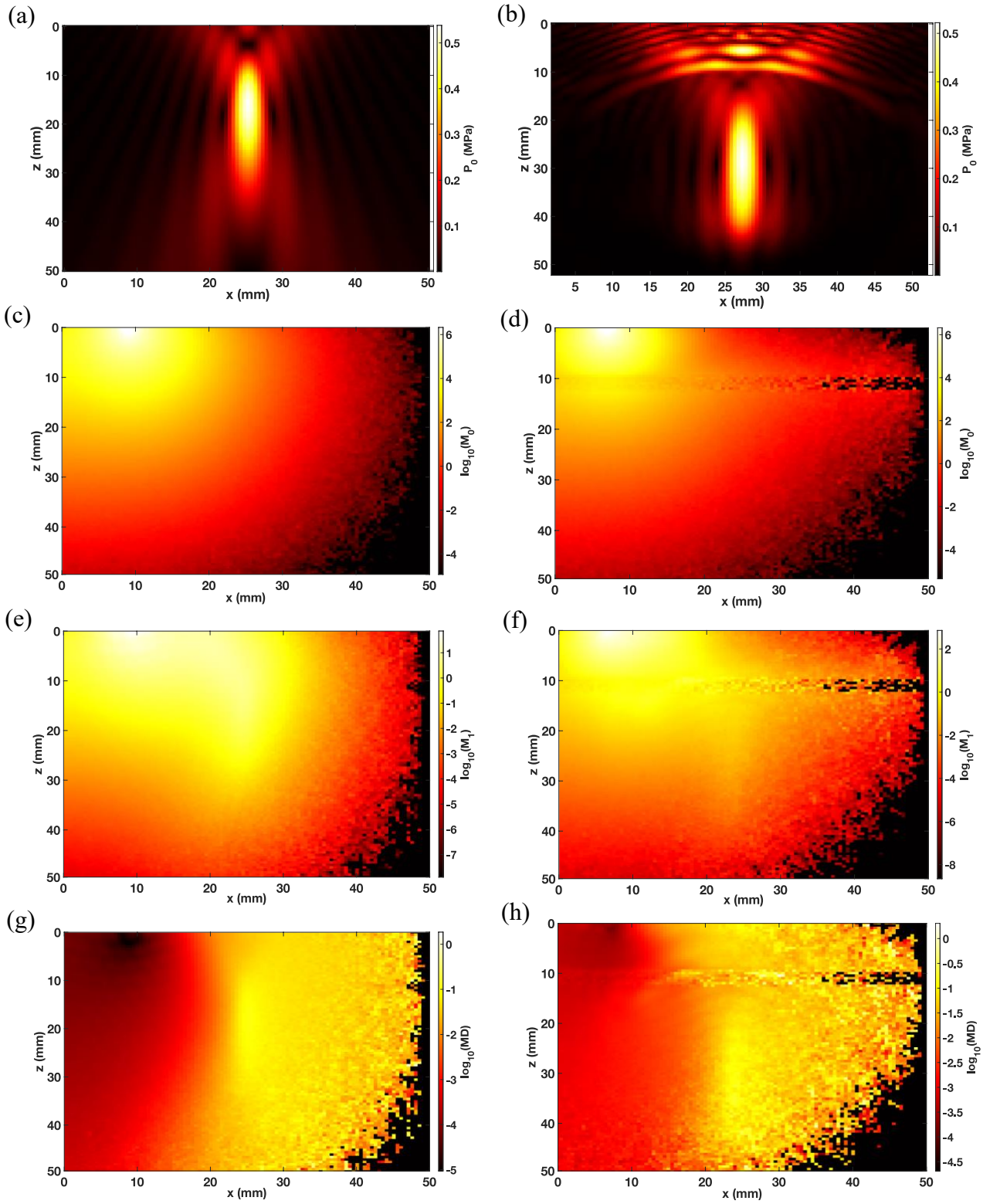

Figure 11 The first column is about the SLB medium and the second column is FLB medium. (a) and (b) is the pressure distribution from a 0.5 MHz FUS transducer. (c) and (d) presents the unmodulated AO fluence distribution where due to homogeneous medium the extent of distribution is more in SLB medium than in FLB medium. (e) and (f) is the modulated AO fluence distribution in SLB and FLB medium, respectively. The modulated light distribution depends on the amount of light intensity interacts the US pressure inside the medium and in FLB less number of photons travelled to the brain medium and so the modulated light at the US focus is less compared to the SLB medium. (g) and (h) presents the MD distribution and FLB medium the MD is present at the scalp, skull, and the brain whereas in SLB medium MD is only at the US focus region.

of the light gets modulated from this region before reaching the US focus part. The modulated light magnitude is less than unity near the focus which is very small compared to the parts near the source. Figure 11 (g) and (h) is the MD distribution which was calculated using Equation 29. In the SLB medium the MD is somewhat maximum at the focus region and is about 2 % - 3 %. Moreover, the value of MD is five orders of magnitudes lower near the source (x = 10 mm) compared to the US focus region. In the FLB medium the MD is higher at the focus but also it is prominent in the scalp and the scull region too. The magnitude of MD at the focus region is around 1% in the FLB medium, and this magnitude decreases 4-4.5 orders of magnitude near the source region. Figure 12 (a) and (b) are the US pressure distribution at 0.9 MHz US in SLB and FLB medium, respectively. Here also the focus was placed at 20 mm and 28 mm in z direction for both mediums. The Figure 12 (c) and (d) are the AO fluence distributions of $M_{0,n}$ of the power spectrum in SLB and FLB medium, respectively. Here also the unmodulated AO fluence is higher near the source for both the cases. Furthermore, the modulated AO fluence ($M_{1,n}$) of the spectrum is also higher at the focus and near the source in the SLB medium but in the FLB medium this is not the case. Here the modulated AO fluence is higher near the source and very small at the focus. In Figure 12 (e) and (f) the MD distribution is shown, here in Figure 12 (g) the MD is higher at the region of US focus and significantly lower near the source region. The magnitude of MD at the US focus is < 1% and near the source MD decreases to 5 orders of magnitude. In Figure 12 (h) the MD distribution is very small at the focus region, and it is also present in the scalp and skull. The magnitude of the MD is < 1% near the focus region and this decreases to 4.5 orders of magnitude near the light source region.

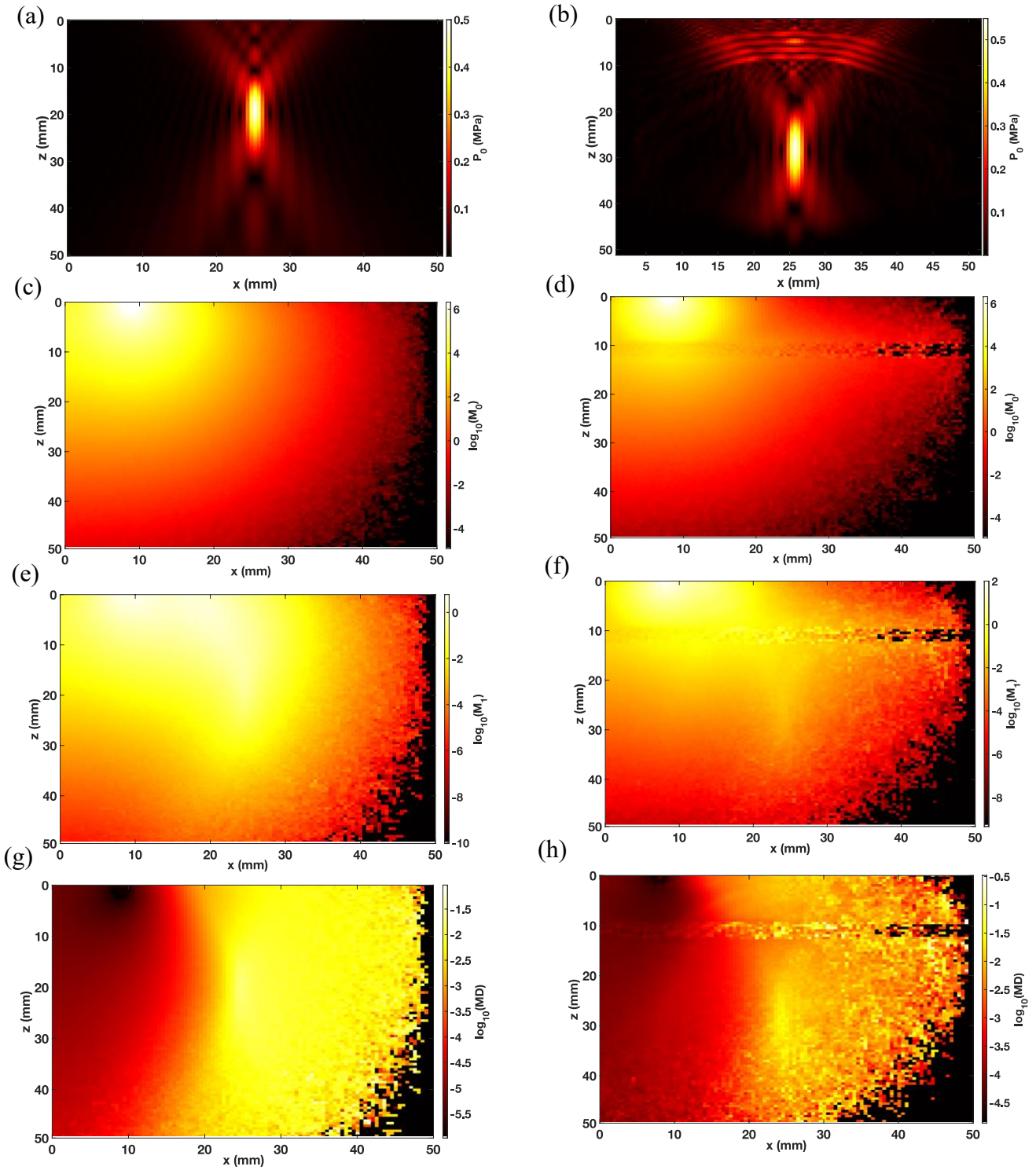

Figure 12 The first column is about the SLB medium, and the second column is FLB medium. (a) and (b) is the pressure distribution from a 0.9 MHz FUS transducer. (c) and (d) presents the unmodulated AO fluence distribution where due to homogeneous medium the extent of distribution is more in SLB medium than in FLB medium. (e) and (f) is the modulated AO fluence distribution in SLB and FLB medium, respectively. The modulated light distribution depends on the amount of light intensity interacts the US pressure inside the medium and in FLB less number of photons travelled to the brain medium and so the modulated light at the US focus is less compared to the SLB medium. (g) and (h) presents the MD distribution and FLB medium the MD is present at the scalp, skull, and the brain whereas in SLB medium MD is only at the US focus region.

5 Discussion

The low-intensity US therapy is the future of targeted drug delivery to the brain, neuroscience studies like neuromodulation, and cancer therapy. However, the lack of real time monitoring is a concern for US therapy. On the other hand, hybrid imaging technique like AO could provide a good contrast at a high penetration depth. This characteristic of AO makes it one of the techniques that could be used for monitoring US therapy. To this end, the thesis presents the first modelling and simulation study of FUS and AO in a FLB medium. The simulation was performed in two steps i.e., first, the acoustic pressure waves from a FUS transducer was simulated on k-Wave MATLAB toolbox and after that, AO-MC model was developed to simulate the ultrasound induced phase shift of light. In all simulations 100 million photons were simulated and the total computation time for AO-MC model was 38 hours.

The US pressure distribution was simulated for FLB medium and SLB medium. The SLB medium was considered as to compare our AO-MC simulation result with FLB medium. The desired pressure at the focus point was 0.5 MPa for all the US simulations. Moreover, at 0.5 MHz the ultrasound transmission was 60% while it was 54% for 0.9 MHz. This shows that for brain therapy the lower frequency US is better in passing across the skull. The US focus elongation is higher in the case of 0.5 MHz and lower at 0.9 MHz. This could be due to skull induced phase change of US waves and the phase change is less for 0.5 MHz than the 0.9 MHz [70]. The k-Wave simulated pressure amplitude, phase, and the direction was loaded in the MC-AO model. The AO-MC model presents the AO fluence distribution of unmodulated and modulated light. The unmodulated light power spectrum is the DC light which has not interacted the US pressure and at both frequencies this distribution is in the region of the light source. In the SLB medium the extent of unmodulated AO fluence distribution is more than the FLB medium because of the inhomogeneity between the two mediums. Furthermore, in the SLB medium, the modulated light distribution for both the frequencies is near the light source and at the US focus region because more amount of light interacted with US focus region. However, the focus region in the FLB medium is located at a depth of 28 mm and due to that, a smaller number of photons are interacting the US focus region. Near the source the modulated light is high because the photon's probability of interaction with US pressure is high near the source. The MD distribution shows the amount of modulated (tagged)

light with respect to DC light. We found out that the MD for 0.5 MHz and 0.9 MHz in SLB medium is very low at places near the light source as the intensity of unmodulated light is very high at these points. As we move near the US focus in SLB medium the modulation depth increases more for 0.5 MHz because of the increase in probability of interaction with US compared to 0.9 MHz focal region. Furthermore, in the FLB medium the MD is low near the focus point compared to the SLB medium. This clearly shows that the signal-to-noise ratio of the measurement depends on the amount of light intensity available and the modulation depth at that region.

5.1 Limitations of this study and future work

The method and derivation used in the AO theory has several limitations and what we intend to do in our future studies are explained below:

i) In k-Wave simulation the different layers of a human head were modeled as concentric semicircles, but the scalp is not uniform and in future, we would work on developing the k-Wave simulations using real human head CT images.

ii) The AO model requires the voxel size to be less than the wavelength of the US. In our case i.e., for 0.5 mm voxel size, this condition is fulfilled but for more accurate model we would require a grid voxel size of 0.1 mm.

iii) While deriving the AO equations we considered that the displacement of scatterers follows the displacement of background medium. However, in future simulations we will try to include the dynamics of the background medium and study its effect on AO phase shifts in photons.

iv) The ultrasound phase modulations are very small and to avoid breaking this assumption, the peak pressure amplitude for all our simulations was normalized to 10 kPa.

v) The accumulation of phase shifts is stored by the method presented in [10] but in our AO-MC the pressure distribution varies at each point of the computational domain, and this causes errors in the phase accumulation.

vi) In our future studies we will develop the voxel-based AO-MC on parallel computation or GPU. Each voxel then would contain the optical, acoustic properties, the pressure magnitude, phase, and direction. Moreover, the

photon’s all events are then calculated inside a single voxel and if it crosses the boundary of the voxel then it will experience new optical or acoustic properties or pressure magnitude, phase properties. This kind of modelling of AO-MC will provide a better accumulation of phase and hence more accurate distribution of MD.

6 Conclusions and Future work

In conclusion, AO effect was studied for US brain therapy by modelling and simulation. First, the US pressure distribution in SLB medium and FLB medium was studied using the k-Wave MATLAB toolbox. We found out that at 0.5 MHz more transmission of US through the skull takes place compared to 0.9 MHz. Second, AO-MC model was developed in MATLAB and the simulated pressure magnitude along with phase and direction matrices was loaded to this model. At each step size and scattering event, the phase shift due to scatterer displacement and refractive index change is accumulated to the current voxel. For both US frequencies, results in SLB medium shows the strong unmodulated light near the source regions and in FLB medium similar phenomenon was seen but the extent of the distribution is small. For the case of modulated light for both the frequencies in SLB medium the distribution is near the source and around the focus region and for the FLB medium near the source region has a strong modulated light distribution than the US focus region. Furthermore, in SLB medium at both US frequencies, the MD distribution is more at the region of US focus, but this MD decreases drastically as we move towards the light source region. In FLB medium the MD at the focus region for both the frequencies is small compared to SLB which shows that the signal-to-noise ratio (SNR) depends not only on MD but also on light intensity present in that region. This result is important for future simulations where we can find optimized position by placing US transducer at different angles to get high SNR of AO modulated light.

7 References

[1] L. V. Wang, “Ultrasound-Mediated Biophotonic Imaging: A Review of Acousto-Optical Tomography and Photo-Acoustic Tomography,” *Disease Markers*, vol. 19, no. 2–3, pp. 123–138, 2004, doi: 10.1155/2004/478079.

[2] D. S. Elson, R. Li, C. Dunsby, R. Eckersley, and M.-X. Tang, “Ultrasound-mediated optical tomography: a review of current methods,” *Interface Focus*, vol. 1, no. 4, pp. 632–648, Aug. 2011, doi: 10.1098/rsfs.2011.0021.

[3] M. Xu and L. v. Wang, “Photoacoustic imaging in biomedicine,” *Review of Scientific Instruments*, vol. 77, no. 4, p. 041101, Apr. 2006, doi: 10.1063/1.2195024.

[4] J. Gunther and S. Andersson-Engels, “Review of current methods of acousto-optical tomography for biomedical applications,” *Frontiers of Optoelectronics*, vol. 10, no. 3, pp. 211–238, Sep. 2017, doi: 10.1007/s12200-017-0718-4.

[5] C. v. Raman and N. S. Nagendra Nathe, “The diffraction of light by high frequency sound waves: Part I,” *Proceedings of the Indian Academy of Sciences - Section A*, vol. 2, no. 4, pp. 406–412, Oct. 1935, doi: 10.1007/BF03035840.

[6] F. A. Marks, H. W. Tomlinson, and G. W. Brooksby, “Comprehensive approach to breast cancer detection using light: photon localization by ultrasound modulation and tissue characterization by spectral discrimination,” *https://doi.org/10.1117/12.154670*, vol. 1888, pp. 500–510, Sep. 1993, doi: 10.1117/12.154670.

[7] L. Wang, S. L. Jacques, and X. Zhao, “Continuous-wave ultrasonic modulation of scattered laser light to image objects in turbid media,” *Optics Letters, Vol. 20, Issue 6, pp. 629-631*, vol. 20, no. 6, pp. 629–631, Mar. 1995, doi: 10.1364/OL.20.000629.

[8] W. Leutz and G. Maret, “Ultrasonic modulation of multiply scattered light,” *Physica B*, vol. 204, pp. 14–19, 1995.

[9] L. v. Wang, “Mechanisms of Ultrasonic Modulation of Multiply Scattered Coherent Light: An Analytic Model,” *Physical Review Letters*, vol. 87, no. 4, p. 043903, Jul. 2001, doi: 10.1103/PhysRevLett.87.043903.

[10] L. v. Wang, “Mechanisms of ultrasonic modulation of multiply scattered coherent light: a Monte Carlo model,” *Optics Letters*, vol. 26, no. 15, p. 1191, Aug. 2001, doi: 10.1364/OL.26.001191.

[11] S. Sakadžić and L. v. Wang, “Ultrasonic modulation of multiply scattered coherent light: An analytical model for anisotropically scattering media,” *Physical Review E*, vol. 66, no. 2, p. 026603, Aug. 2002, doi: 10.1103/PhysRevE.66.026603.

[12] S. Sakadžić and L. v. Wang, “Modulation of multiply scattered coherent light by ultrasonic pulses: An analytical model,” *Physical Review E*, vol. 72, no. 3, p. 036620, Sep. 2005, doi: 10.1103/PhysRevE.72.036620.

[13] P. Lai, J. R. McLaughlan, A. B. Draudt, T. W. Murray, R. O. Cleveland, and R. A. Roy, “Real-Time Monitoring of High-Intensity Focused Ultrasound Lesion Formation Using Acousto-Optic Sensing,” *Ultrasound in Medicine & Biology*, vol. 37, no. 2, pp. 239–252, Feb. 2011, doi: 10.1016/j.ultrasmedbio.2010.11.004.

[14] K. Daoudi, A. Hussain, E. Hondebrink, and W. Steenbergen, “Correcting photoacoustic signals for fluence variations using acousto-optic modulation,” *Optics Express*, vol. 20, no. 13, p. 14117, Jun. 2012, doi: 10.1364/OE.20.014117.

[15] M. Rosenfeld, G. Weinberg, D. Doktofsky, Y. Li, L. Tian, and O. Katz, “Acousto-optic ptychography,” *Optica*, vol. 8, no. 6, p. 936, Jun. 2021, doi: 10.1364/OPTICA.424828.

[16] D. Doktofsky, M. Rosenfeld, and O. Katz, “Acousto optic imaging beyond the acoustic diffraction limit using speckle decorrelation,” *Communications Physics*, vol. 3, no. 1, p. 5, Dec. 2020, doi: 10.1038/s42005-019-0267-9.

[17] M. Jang, H. Ko, J. H. Hong, W. K. Lee, J.-S. Lee, and W. Choi, “Deep tissue space-gated microscopy via acousto-optic interaction,” *Nature Communications*, vol. 11, no. 1, p. 710, Dec. 2020, doi: 10.1038/s41467-020-14514-7.

[18] Y. Liu, R. Cao, J. Xu, H. Ruan, and C. Yang, “Imaging through highly scattering human skulls with ultrasound-modulated optical tomography,” *Optics Letters*, vol. 45, no. 11, p. 2973, Jun. 2020, doi: 10.1364/OL.390920.

[19] M. B. Robinson, S. A. Carp, A. Peruch, D. A. Boas, M. A. Franceschini, and S. Sakadžić, “Characterization of continuous wave ultrasound for acousto-optic

modulated diffuse correlation spectroscopy (AOM-DCS)," *Biomedical Optics Express*, vol. 11, no. 6, p. 3071, Jun. 2020, doi: 10.1364/BOE.390322.

[20] A. Hussain, W. Steenbergen, and I. M. Vellekoop, "Imaging blood flow inside highly scattering media using ultrasound modulated optical tomography," *Journal of Biophotonics*, vol. 11, no. 1, p. e201700013, Jan. 2018, doi: 10.1002/jbio.201700013.

[21] I. Donald, J. Macvicar, and T. G. Brown, "Investigation of abdominal masses by pulsed ultrasound," *Lancet*, vol. 1, no. 7032, pp. 1188–1195, Jun. 1958, doi: 10.1016/S0140-6736(58)91905-6.

[22] T. L. Szabo, "Diagnostic Ultrasound Imaging: Inside Out: Second Edition," *Diagnostic Ultrasound Imaging: Inside Out: Second Edition*, pp. 1–549, 2004, doi: 10.1016/C2011-0-07261-7.

[23] T. Conner-Kerr and M. E. Oesterle, "Current perspectives on therapeutic ultrasound in the management of chronic wounds: a review of evidence," *Chronic Wound Care Management and Research*, vol. 4, pp. 89–98, Jul. 2017, doi: 10.2147/CWCMR.S135982.

[24] E. L. Nussbaum, "Ultrasound: to heat or not to heat—that is the question," *http://dx.doi.org/10.1179/ptr.1997.2.2.59*, vol. 2, no. 2, pp. 59–72, Jun. 2013, doi: 10.1179/PTR.1997.2.2.59.

[25] M. Snehota, J. Vachutka, G. ter Haar, L. Dolezal, and H. Kolarova, "Therapeutic ultrasound experiments in vitro: Review of factors influencing outcomes and reproducibility," *Ultrasonics*, vol. 107, p. 106167, Sep. 2020, doi: 10.1016/J.ULTRAS.2020.106167.

[26] Z. Izadifar, P. Babyn, and D. Chapman, "Mechanical and Biological Effects of Ultrasound: A Review of Present Knowledge," *Ultrasound Med Biol*, vol. 43, no. 6, pp. 1085–1104, Jun. 2017, doi: 10.1016/J.ULTRASMEDBIO.2017.01.023.

[27] Z. Izadifar, Z. Izadifar, D. Chapman, and P. Babyn, "An Introduction to High Intensity Focused Ultrasound: Systematic Review on Principles, Devices, and Clinical Applications," *J Clin Med*, vol. 9, no. 2, Feb. 2020, doi: 10.3390/JCM9020460.

[28] K. Daoudi *et al.*, “In vivo photoacoustics and high frequency ultrasound imaging of mechanical high intensity focused ultrasound (HIFU) ablation,” *Biomed Opt Express*, vol. 8, no. 4, p. 2235, Apr. 2017, doi: 10.1364/BOE.8.002235.

[29] J. P. Gray, N. Dana, K. L. Dextraze, F. Maier, S. Emelianov, and R. R. Bouchard, “Multi-Wavelength Photoacoustic Visualization of High Intensity Focused Ultrasound Lesions,” *Ultrason Imaging*, vol. 38, no. 1, pp. 96–112, Jan. 2016, doi: 10.1177/0161734615593747.

[30] M. T. Adams, R. O. Cleveland, and R. A. Roy, “Treatment planning and strategies for acousto-optic guided high-intensity focused ultrasound therapies,” *J Acoust Soc Am*, vol. 135, no. 4, p. 2267, May 2014, doi: 10.1121/1.4877433.

[31] W. Lopez *et al.*, “Ultrasound Therapy, Chemotherapy and Their Combination for Prostate Cancer,” *Technol Cancer Res Treat*, vol. 20, Jan. 2021, doi: 10.1177/15330338211011965.

[32] A. Burgess and K. Hynynen, “Noninvasive and targeted drug delivery to the brain using focused ultrasound,” *ACS Chem Neurosci*, vol. 4, no. 4, pp. 519–526, Apr. 2013, doi: 10.1021/CN300191B.

[33] D. McMahon, M. A. O’Reilly, and K. Hynynen, “Therapeutic Agent Delivery Across the Blood-Brain Barrier Using Focused Ultrasound,” *Annu Rev Biomed Eng*, vol. 23, pp. 89–113, Jul. 2021, doi: 10.1146/ANNUREV-BIOENG-062117-121238.

[34] P. C. Klink *et al.*, “Combining brain perturbation and neuroimaging in non-human primates,” *Neuroimage*, vol. 235, Jul. 2021, doi: 10.1016/J.NEUROIMAGE.2021.118017.

[35] K. Hynynen, N. McDannold, N. Vykhodtseva, and F. A. Jolesz, “Noninvasive MR imaging-guided focal opening of the blood-brain barrier in rabbits,” *Radiology*, vol. 220, no. 3, pp. 640–646, 2001, doi: 10.1148/RADIOL.2202001804.

[36] I. Manzoor, R. Bacha, and S. A. Gilani, “Applications of High-Intensity Focused Ultrasound in the Treatment of Different Pathologies:,” *https://doi.org/10.1177/8756479320972086*, vol. 37, no. 2, pp. 171–178, Dec. 2020, doi: 10.1177/8756479320972086.

[37] D. P. Darrow, “Focused Ultrasound for Neuromodulation,” *Neurotherapeutics*, vol. 16, no. 1, pp. 88–99, Jan. 2019, doi: 10.1007/S13311-018-00691-3.

[38] C. Gasca-Salas *et al.*, “Blood-brain barrier opening with focused ultrasound in Parkinson’s disease dementia,” *Nat Commun*, vol. 12, no. 1, Dec. 2021, doi: 10.1038/S41467-021-21022-9.

[39] Y. Meng, K. Hynynen, and N. Lipsman, “Applications of focused ultrasound in the brain: from thermoablation to drug delivery,” *Nat Rev Neurol*, vol. 17, no. 1, pp. 7–22, Jan. 2021, doi: 10.1038/S41582-020-00418-Z.

[40] Y. Meng, K. Hynynen, and N. Lipsman, “Applications of focused ultrasound in the brain: from thermoablation to drug delivery,” *Nat Rev Neurol*, vol. 17, no. 1, pp. 7–22, Jan. 2021, doi: 10.1038/S41582-020-00418-Z.

[41] S. G. Resink, “State-of-the art of acousto-optic sensing and imaging of turbid media,” *Journal of Biomedical Optics*, vol. 17, no. 4, p. 040901, Apr. 2012, doi: 10.1117/1.JBO.17.4.040901.

[42] Y. Huang, M. Cua, J. Brake, Y. Liu, and C. Yang, “Investigating ultrasound–light interaction in scattering media,” *Journal of Biomedical Optics*, vol. 25, no. 02, p. 1, Feb. 2020, doi: 10.1117/1.JBO.25.2.025002.

[43] R. Zemp, S. Sakadžić, and L. v. Wang, “Stochastic explanation of speckle contrast detection in ultrasound-modulated optical tomography,” *Physical Review E*, vol. 73, no. 6, p. 061920, Jun. 2006, doi: 10.1103/PhysRevE.73.061920.

[44] T. S. Leung and S. Powell, “Fast Monte Carlo simulations of ultrasound-modulated light using a graphics processing unit,” *Journal of Biomedical Optics*, vol. 15, no. 5, p. 055007, 2010, doi: 10.1117/1.3495729.

[45] M. T. Adams, R. O. Cleveland, and R. A. Roy, “Modeling-based design and assessment of an acousto-optic guided high-intensity focused ultrasound system,” *Journal of Biomedical Optics*, vol. 22, no. 1, p. 017001, Jan. 2017, doi: 10.1117/1.JBO.22.1.017001.

[46] J. Honeysett, E. Stride, and T. Leung, “Monte Carlo simulations of acousto-optics with microbubbles,” Feb. 2010, p. 75640K. doi: 10.1117/12.842030.

[47] J. E. Honeysett, E. Stride, and T. S. Leung, “Feasibility Study of Non-invasive Oxygenation Measurement in a Deep Blood Vessel Using Acousto-Optics and Microbubbles,” 2012, pp. 277–283. doi: 10.1007/978-1-4614-1566-4_41.

[48] A. Levi, S. Monin, E. Hahamovich, A. Lev, B. G. Sfez, and A. Rosenthal, "Increased SNR in acousto-optic imaging via coded ultrasound transmission," *Optics Letters*, vol. 45, no. 10, p. 2858, May 2020, doi: 10.1364/OL.392617.

[49] Z. Cheng and L. v. Wang, "Focusing light into scattering media with ultrasound-induced field perturbation," *Light: Science & Applications*, vol. 10, no. 1, p. 159, Dec. 2021, doi: 10.1038/s41377-021-00605-7.

[50] F. Ramaz, J.-M. Tualle, L. Dutheil, M. Bocoum, M. Fink, and S. M. Popoff, "Fourier transform acousto-optic imaging with off-axis holographic detection," *Applied Optics, Vol. 60, Issue 24, pp. 7107-7112*, vol. 60, no. 24, pp. 7107–7112, Aug. 2021, doi: 10.1364/AO.427181.

[51] F. J. Chung and J. C. Schotland, "Inverse Transport and Acousto-Optic Imaging," *SIAM Journal on Mathematical Analysis*, vol. 49, no. 6, pp. 4704–4721, Jan. 2017, doi: 10.1137/16M1104767.

[52] F. J. Chung, J. G. Hoskins, and J. C. Schotland, "A Transport Model for Multi-Frequency Acousto-Optic Tomography," Oct. 2019.

[53] F. J. Chung, R.-Y. Lai, and Q. Li, "On diffusive scaling in acousto-optic imaging," *Inverse Problems*, vol. 36, no. 8, p. 085011, Aug. 2020, doi: 10.1088/1361-6420/ab9f85.

[54] E.-Y. Park, J. Baik, H. Kim, S.-M. Park, and C. Kim, "Ultrasound-modulated optical glucose sensing using a 1645 nm laser," *Scientific Reports*, vol. 10, no. 1, p. 13361, Dec. 2020, doi: 10.1038/s41598-020-70305-6.

[55] F. S. Pavone and S. Shoham, *Handbook of Neurophotonics*. First edition. | Boca Raton, FL : CRC Press, 2020. | Series: Series in cellular and clinical imaging: CRC Press, 2020. doi: 10.1201/9780429194702.

[56] B. E. Treeby and B. T. Cox, "k-Wave: MATLAB toolbox for the simulation and reconstruction of photoacoustic wave fields," *J Biomed Opt*, vol. 15, no. 2, p. 021314, 2010, doi: 10.1117/1.3360308.

[57] E. S. Wise, B. T. Cox, J. Jaros, and B. E. Treeby, "Representing arbitrary acoustic source and sensor distributions in Fourier collocation methods a)," 2019, doi: 10.1121/1.5116132.

[58] A. N. Pouliopoulos, S. Y. Wu, M. T. Burgess, M. E. Karakatsani, H. A. S. Kamimura, and E. E. Konofagou, "A Clinical System for Non-invasive Blood-

Brain Barrier Opening Using a Neuronavigation-Guided Single-Element Focused Ultrasound Transducer," *Ultrasound Med Biol*, vol. 46, no. 1, pp. 73–89, Jan. 2020, doi: 10.1016/J.ULTRASMEDBIO.2019.09.010.

[59] H. T. O'Neil, "Theory of Focusing Radiators," *J Acoust Soc Am*, vol. 21, no. 5, p. 516, Jun. 2005, doi: 10.1121/1.1906542.

[60] J. Schäfer and A. Kienle, "Scattering of light by multiple dielectric cylinders: comparison of radiative transfer and Maxwell theory," *OPTICS LETTERS*, vol. 15, no. 20, p. 2413, 2008.

[61] A. Kienle and M. S. Patterson, "Improved solutions of the steady-state and the time-resolved diffusion equations for reflectance from a semi-infinite turbid medium," *JOSA A, Vol. 14, Issue 1, pp. 246-254*, vol. 14, no. 1, pp. 246–254, Jan. 1997, doi: 10.1364/JOSAA.14.000246.

[62] L. Wang, S. L. Jacques, and L. Zheng, "MCML-Monte Carlo modeling of light transport in multi-layered tissues," *Computer Methods and Programs in Biomedicine*, vol. 47, no. 2, pp. 131–146, 1995, doi: 10.1016/0169-2607(95)01640-F.

[63] Q. Fang *et al.*, "Monte Carlo Simulation of Photon Migration in 3D Turbid Media Accelerated by Graphics Processing Units," *Optics Express, Vol. 17, Issue 22, pp. 20178-20190*, vol. 17, no. 22, pp. 20178–20190, Oct. 2009, doi: 10.1364/OE.17.020178.

[64] X. Fang, B. Pan, W. Liu, Z. Wang, and T. Li, "Effect of Scalp Hair Follicles on NIRS Quantification by Monte Carlo Simulation and Visible Chinese Human Dataset," *IEEE Photonics Journal*, vol. 10, no. 5, Oct. 2018, doi: 10.1109/JPHOT.2018.2865427.

[65] S. Sakadžić and L. v. Wang, "Correlation transfer equation for ultrasound-modulated multiply scattered light," *Physical Review E - Statistical, Nonlinear, and Soft Matter Physics*, vol. 74, no. 3, p. 036618, Sep. 2006, doi: 10.1103/PHYSREVE.74.036618/FIGURES/3/MEDIUM.

[66] S. Sakadžić and L. v. Wang, "Correlation transfer and diffusion of ultrasound-modulated multiply scattered light," *Physical Review Letters*, vol. 96, no. 16, p. 163902, Apr. 2006, doi: 10.1103/PHYSREVLETT.96.163902/FIGURES/1/MEDIUM.

[67] M. T. Adams, “A modeling-based assessment of acousto-optic sensing for monitoring high-intensity focused ultrasound lesion formation,” Doctor of Philosophy, Boston University, 2015.

[68] F. J. Blonigen *et al.*, “Computations of the acoustically induced phase shifts of optical paths in acoustophotonic imaging with photorefractive-based detection,” *Applied Optics, Vol. 44, Issue 18, pp. 3735-3746*, vol. 44, no. 18, pp. 3735–3746, Jun. 2005, doi: 10.1364/AO.44.003735.

[69] J. Shin *et al.*, “Focused ultrasound-mediated noninvasive blood-brain barrier modulation: preclinical examination of efficacy and safety in various sonication parameters,” *Neurosurg Focus*, vol. 44, no. 2, 2018, doi: 10.3171/2017.11.FOCUS17627.

[70] J. Sun and K. Hynynen, “Focusing of therapeutic ultrasound through a human skull: A numerical study,” *J Acoust Soc Am*, vol. 104, no. 3, p. 1705, Oct. 1998, doi: 10.1121/1.424383.

[71] L. v. Wang, “Mechanisms of ultrasonic modulation of multiply scattered coherent light: an analytic model,” *Phys Rev Lett*, vol. 87, no. 4, pp. 43903-1-43903–4, Jul. 2001, doi: 10.1103/PHYSREVLETT.87.043903.

[72] “NaviFUS - Neuronavigation-guided focused ultrasound system.” https://navifus.com/ (accessed May 12, 2022).